REPORT DOCUMENTATION PAGE

Form Approved
OMB No. 0704-0188

1. REPORT DATE *(DD-MM-YYYY)*	**2. REPORT TYPE**	**3. DATES COVERED** *(From - To)*
05-09-2014		

4. TITLE AND SUBTITLE

Sonic Actuation of Small-Scale Robots in a Fluidic Environment

5a. CONTRACT NUMBER

5b. GRANT NUMBER

5c. PROGRAM ELEMENT NUMBER

6. AUTHOR(S)
House, Christopher Brian

5d. PROJECT NUMBER

5e. TASK NUMBER

5f. WORK UNIT NUMBER

7. PERFORMING ORGANIZATION NAME(S) AND ADDRESS(ES)

8. PERFORMING ORGANIZATION REPORT NUMBER

9. SPONSORING / MONITORING AGENCY NAME(S) AND ADDRESS(ES)
U.S. Naval Academy
Annapolis, MD 21402

10. SPONSOR/MONITOR'S ACRONYM(S)

11. SPONSOR/MONITOR'S REPORT NUMBER(S)
Trident Scholar Report no. 428 (2014)

12. DISTRIBUTION / AVAILABILITY STATEMENT

This document has been approved for public release; its distribution is UNLIMITED.

13. SUPPLEMENTARY NOTES

14. ABSTRACT

Microrobotics represents an important development in technology that has vast applications, particularly in medical fields. Some challenges with these systems include the method of propulsion, control, and power delivery for the device. Many groups are currently developing magnetically based actuation methods but this project focusses on an alternative method of actuation in which acoustic waves would excite the robot structure to resonance, thus propelling and steering the robot. The actuation focuses on the development of a double-jointed, flagella-like, flapper designed for non-reciprocal motion. Unlike reciprocal motion, non-reciprocal motion has a time irreversible nature, causing displacement regardless of the surrounding environment. Such motion is essential for microscale propulsion, where surface forces dominate inertial forces. Since the flapper uses a resonance mode, it is also frequency selective; this could allow for future steering capability by using multiple flagella tuned to different frequencies. The flapper mechanism was tested in a high viscosity fluid to reproduce the low Reynolds number environment of microrobotics. The contribution of this project would be the demonstration of a novel form of microscale propulsion using acoustic radiation forces to drive mechanical flappers to resonance, creating non-reciprocal motion. This novel form of actuation would be extendable to future microrobot applications, to include *in vivo* medical applications such as non-invasive surgery, targeted drug delivery, and telemetry.

15. SUBJECT TERMS
Microrobotics, COMSOL, acoustic field, non-reciprocal motion, low Reynolds number

16. SECURITY CLASSIFICATION OF:			**17. LIMITATION OF ABSTRACT**	**18. NUMBER OF PAGES**	**19a. NAME OF RESPONSIBLE PERSON**
a. REPORT	**b. ABSTRACT**	**c. THIS PAGE**		38	**19b. TELEPHONE NUMBER** *(include area code)*

U.S.N.A. --- Trident Scholar project report; no. 428 (2014)

SONIC ACTUATION OF SMALL-SCALE ROBOTS IN A FLUIDIC ENVIRONMENT

by

Midshipman 1/C Christopher B. House
United States Naval Academy
Annapolis, Maryland

Certification of Adviser(s) Approval

Professor Samara L. Firebaugh
Electrical and Computer Engineering Department

Associate Professor Jenelle A. Piepmeier
Weapons and Systems Engineering Department

Associate Professor John A. Burkhardt
Mechanical Engineering Department

Acceptance for the Trident Scholar Committee

Professor Maria J. Schroeder
Associate Director of Midshipman Research

USNA-1531-2

Abstract

Microrobotics represents an important development in technology that has vast applications, particularly in medical fields. Some challenges with these systems include the method of propulsion, control, and power delivery for the device. Many groups are currently developing magnetically based actuation methods, either to create a pulling drive, oscillatory motion, or a corkscrew motion. These magnetically based systems tend to be inefficient and could potentially lead to undesirable effects on the human body. This project is focusing on an alternative method of actuation in which acoustic waves would excite the robot structure to resonance, thus propelling and steering the robot. Acoustic control provides an interesting alternative to existing magnetic or electrostatic actuation in that acoustic signals produce few harmful effects on the human subject. Furthermore, the use of acoustic signals allows for the possibility to leverage existing medical imaging technology. This project focuses on the development of a double-jointed, flagella-like, flapper designed for non-reciprocal motion. Unlike reciprocal motion, non-reciprocal motion has a time irreversible nature, causing displacement regardless of the surrounding environment. Such motion is essential for microscale propulsion, where surface forces dominate inertial forces. Since the flapper uses a resonance mode, it is also frequency selective; this could allow for future steering capability by using multiple flagella tuned to different frequencies. The flapper mechanism was tested in a high viscosity fluid to reproduce the low Reynolds number environment of microrobotics. The contribution of this project would be the demonstration of a novel form of microscale propulsion using acoustic radiation forces to drive mechanical flappers to resonance, creating non-reciprocal motion. This novel form of actuation would be extendable to future microrobot applications, to include *in vivo* medical applications such as non-invasive surgery, targeted drug delivery, and telemetry.

Keywords: Microrobotics, COMSOL, acoustic field, non-reciprocal motion, low Reynolds number

Acknowledgements

This Trident project has been a great experience and with all opportunities like the Trident scholarship, I would be remiss without thanking those who made it possible. First, I would like to thank my advisors: Professor Samara Firebaugh, Professor Jenelle Piepmeier, and Professor John Burkhardt, for their guidance over the last year and a half. They have helped me to shape the project into a successful venture, and I certainly would not have accomplished much without their help. I would also like to thank the Trident committee and Professor Schroeder for granting me the opportunity to be a Trident scholar.

I would like to thank Professor Bishop for his assistance in helping me fabricate the robots and lending me some of his equipment, the electrical engineering, systems engineering, mechanical engineering techs for helping out with various support roles, and the Computer Support Branch (CSB) for their technical assistance throughout the project.

Finally, I would like to thank Major Woodward, USMC, 19th Company Officer, Professor Craig Whitaker, Professor Hau Ngo, MIDN 1/C Jean-Luc Currie, and MIDN 1/C John Nowell, for their support in my selection as a Trident Scholar.

Table of Contents

I. Introduction

Microrobotics is a field that holds great potential for future discovery. Scientists have been exploring the option of using microrobots in various medical fields, such as surgery, oncology, and diagnostic medicine, in order to better treat patients. The field holds many promising advantages, namely that, as Feynman stated, it allows the doctor to be placed "inside" of the patient [1]. Microrobotics, particularly because of their diminutive nature, can be used for targeted therapy, telemetry, and surgical actions [2].

Two of the biggest issues facing microrobotics are power transfer and propulsion. Conventional robots are generally designed with compartmentalized sections, such as motors and batteries, for power, control, and other functions [3]. However, a microrobot, due to its much smaller scale, cannot afford to have too much space devoted to a single function. Also, at the microscale, the viscous forces on the robot dominate over inertial forces, so that macroscopic propulsion mechanisms that use traditional reciprocal motion, such as a stiff oar, are ineffective [4]. Reciprocal motion occurs when a movement is undone by the reverse movement. Such motion does not allow for propulsion in respect to swimmers with a high-drag-to-inertia ratio, because such devices have no "glide" in their motion. Non-reciprocal motion must be used, where the "return stroke" is not simply the reverse of the forward stroke. Examples of non-reciprocal actuators include bacteria flagella, rotating helical coils, and ultrasonic thrusters [5][6].

A number of groups have developed microrobots that utilize magnetic fields for control and actuation [7][8]. One technique that has been successfully developed is to create a rotating magnetic field that pulls a corkscrew type apparatus through a fluid, creating a flagellar motion similar to *E. Coli* [9]. This method of propulsion creates the necessary non-reciprocal motion that is required for small scale propulsion, discussed in more detail below. A disadvantage with magnetics-based methods is that the range of frequencies used can be harmful over time to the human body. This project explores the alternative of powering a swimming microrobot through acoustic energy. Some microrobots have utilized ultrasonic thrusters, where the microrobot is subjected to ultrasonic waves and a corresponding jet of water at the tail end of the robot propels it forward [6][10]. Others have used piezoelectric actuators powered by ultrasonic waves to drive the microrobot at resonant frequencies [11]. Any of these methods provides advantages over other forms of powering the robot due to the use of ultrasound as opposed to electrostatic or electromagnetic waves. Ultrasound is less harmful to the human body and is commonly used in medical applications. In this project, a novel method of acoustic actuation is explored, using a double-jointed flapper designed to resonate in a manner similar to bacteria's flagella.

II. Theory

A key issue in designing a swimming microrobot is its propulsion system. The Reynolds number, *Re*, which is a measure of the effect of inertial forces over viscous forces, is used to classify the flow regime for different systems. It is given by

$$Re = \frac{\rho \cdot v \cdot L}{\mu} \tag{1}$$

where ρ is the density, v is the velocity, L is the characteristic length of the object and μ is the

dynamic viscosity. Microscale objects moving in water[1] or similar fluids typically have very low Reynolds numbers, of the order of 0.1 or less.

For Re << 1, the characteristic fluid flow develops into Stokes' Flow, also called "creeping flow," due to the very slow nature of the fluid flow around the object. A comparable analogy to Stokes' Flow is for a human to attempt to swim through a pool of molasses. For such a low Reynolds Number, the inertial forces acting on the submerged object are essentially negligible. Using the Navier-Stokes equation, it can be shown that the drag force on a submerged object is proportional to its velocity, and furthermore, the object can only move by the action of external forces.

$$\rho\left(\frac{d\vec{v}}{dt} + \vec{v}\cdot\nabla\vec{v}\right) = -\nabla P + \mu\cdot\nabla^2\vec{v} + \vec{F} \quad (2)$$

In Equation 2, the left side of the equation represents the inertial terms, and for Re << 1 can be simplified to zero. Thus, for creeping flow, the resulting equation is

$$\nabla P = \mu\cdot\nabla^2\vec{v} + \vec{F} \quad (3)$$

Table 1 shows a comparison of Reynolds numbers of different scale sizes of robots submerged in different fluids. While the eventual goal for this work is a microscale robot that would operate in fluids like water or blood, the use of more viscous fluids would allow for a milli-scale robot to operate in the same fluid regime. This is beneficial as it is easier to fabricate and test robots at the milliscale, allowing for more rapid prototyping.

Table 1: Comparison of expected Reynolds Numbers for micro- and milliscale robots in different fluids. Note how the use of a highly viscous fluid reduces the Reynolds number for the milliscale device.

Robot Scale	**Fluid**	L **(m)**	ρ **(25°C) (kg/m^3)**	v **(m/s)**	μ **(25°C) (Pa·s)**	Re
Micro	Water	100×10^{-6}	997	1×10^{-3}	8.90×10^{-4}	0.1120
Milli	Water	1×10^{-3}	997	0.1	8.90×10^{-4}	112.0225
Milli	Honey	1×10^{-3}	1360	0.1	0.4	0.3400
Milli	Castor Oil	1×10^{-3}	960	0.1	0.65	0.1476

[1] Water has a density of $\rho = 997$ kg/m^3 and dynamic viscosity of $\mu = 8.90 \times 10^{-4}$ Pa·s, at 25° C

At this point, the idea of reciprocal motion must be more fully explained. Reciprocal motion refers to "changing the [object] into a certain shape and then…going back to the original shape by going through the sequence in reverse" [12]. With conditions indicating Stokes' Flow, reciprocal motion does not allow for any movement or change of position. Essentially, for an object with low Reynolds number, since the viscous forces acting on the object are much stronger than the inertial forces, any reciprocal motion made by the object simply cancels out, for zero net displacement. For such an object, say a spherical object with a flapping tail, to be able to propel itself, the tail must have two or more joints, as shown in Figure 1 [12]. Furthermore, the motion must not be a reversible pattern, like the top section in Figure 2. It must be a pattern that cannot be reversed, similar to the bottom section of Figure 2, in order for non-reciprocal motion to occur.

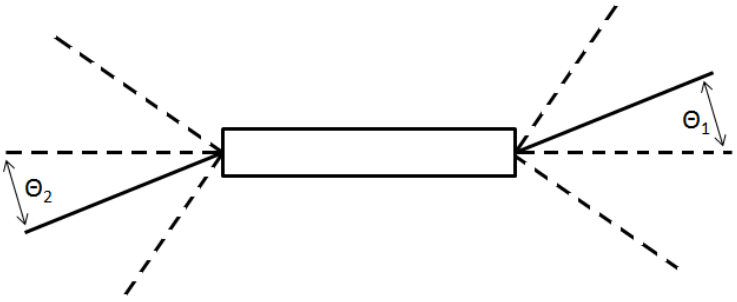

Figure 1: A double-jointed flapper, allowing for non-reciprocal motion [12].

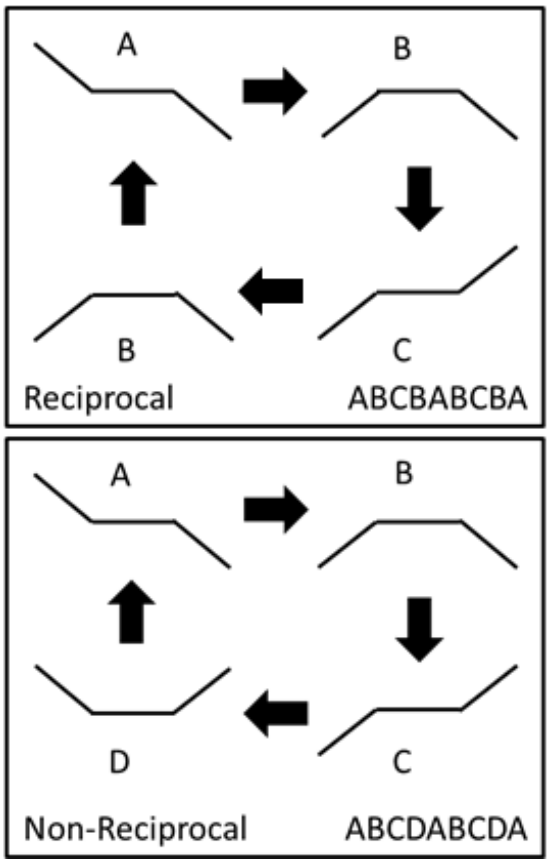

Figure 2: A comparison between reciprocal and non-reciprocal motion for the previous figure [13].

To understand why non-reciprocal motion causes linear movement, imagine a human rowing a boat in molasses with a flexible oar, such as that of Figure 3. If the oars were stiff (and not lifted out of the fluid after each pull), the initial pull would simply be reversed by the rower's next push, and the boat would not move. However, once the rower completes his initial pull, the flexible oar bends in the opposite manner, creating asymmetrical movement, which is the necessary condition for non-reciprocal motion. This actually propels the boat forward since it cannot be reversed by the fluid's viscous forces.

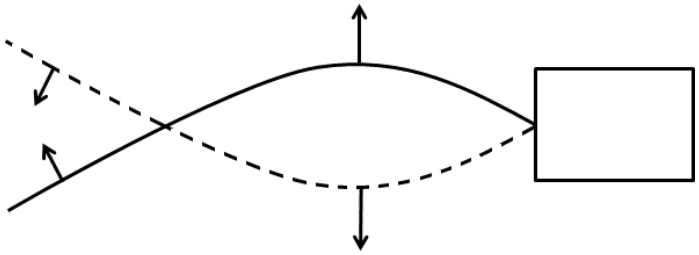

Figure 3: A flexible oar exhibiting non-reciprocal motion [12].

Figure 4 represents a 3-D model that is a rough estimate of the robot design. In order to fully understand the motion of the double-jointed flapper, initial testing began with a clamped version of the flapper, displayed in Figure 5. In order to model this double-jointed flapper design, an analogous system was analyzed. The analogous system involves two cantilever beams bending like a diving board. Figure 6 shows a cantilever beam system with a single mass bending like a diving board. Figures 7 and 8 display a cantilever beam system with two masses and the corresponding pattern for non-reciprocal motion.

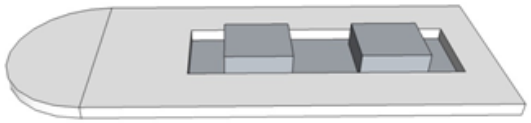

Figure 4: A 3-D model of the initial proposed design.

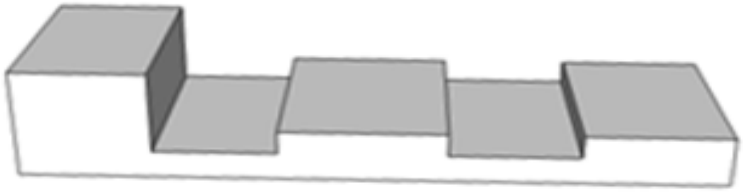

Figure 5: A 3-D model of the proposed flapper, where the raised sections represent the masses in the equivalent spring-mass system.

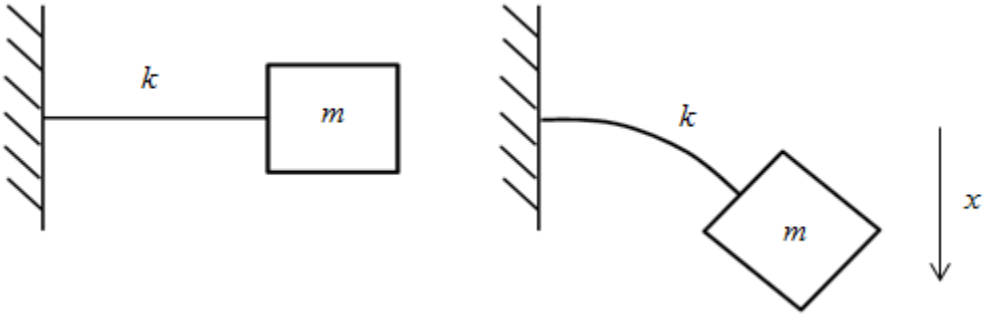

Figure 6: A cantilever beam with mass m, spring constant k, and displacement x bending similarly to a diving board.

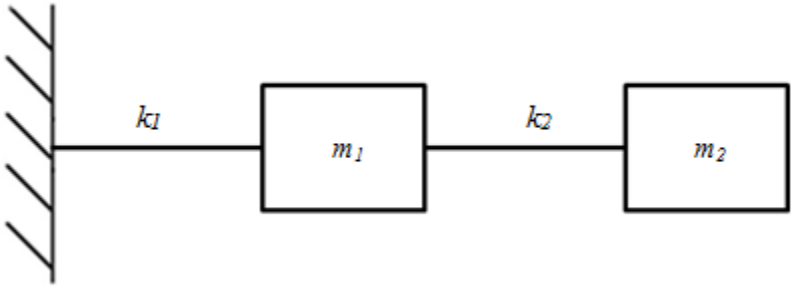

Figure 7: A cantilever beam system with two masses, m_1 and m_2, and spring constants, k_1 and k_2.

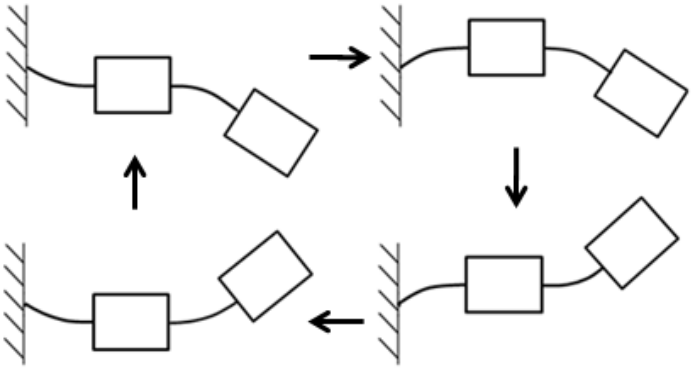

Figure 8: The cantilever beam system displaying non-reciprocal motion.

The double cantilever beam system, shown in Figures 7 and 8, is analogous to a spring-mass system with two masses connected by two springs, as shown in Figure 9.

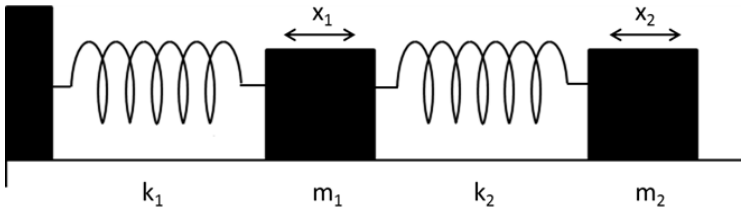

Figure 9: A coupled spring-mass system with two degrees of freedom [14].

The analysis of such a system involves utilizing Newton's Second Law in combination with Hooke's Law, as shown in Equation 4:

$$F_{net} = m \cdot x'' = -k \cdot x \tag{4}$$

The variable *m* corresponds with mass, *k* with the spring constants, and *x* with the horizontal displacement. Since the system is coupled, a system of differential equations results, shown in Equations 5 and 6:

$$m_1 x_1'' = -k_1 x_1 + k_2(x_2 + x_1) \tag{5}$$

$$m_2 x_2'' = -k_2(x_2 + x_1) \tag{6}$$

In matrix form, this is equivalent to the following:

$$\boldsymbol{MX'' + KX = 0} \tag{7}$$

To solve this, harmonic motion must be assumed by letting $\boldsymbol{x_i = X_i e^{j\omega t}}$. After some manipulation, the system can be rearranged to the following form:

$$\boldsymbol{(M^{-1}K - \omega^2 I)X = 0} \tag{8}$$

After setting the determinant of this coefficient matrix equal to 0, the characteristic equation for the system is obtained (where $\omega^2 = \lambda$):

$$\lambda^2 - b\lambda + c = 0 \tag{9}$$

In this equation, b and c are composed of the two spring constants, k_1 and k_2, and the two masses, m_1 and m_2. The corresponding roots of this quadratic equation give the eigenvalues, or eigenfrequencies in this case, which are the system's resonant frequencies. These are summarized in Equation 10:

$$\lambda = \frac{\frac{k_1+k_2}{m_1}+\frac{k_2}{m_2} \pm \sqrt{\left(\frac{k_1+k_2}{m_1}+\frac{k_2}{m_2}\right)^2 - 4\left(\frac{k_1 k_2}{m_1 m_2}\right)}}{2} \tag{10}$$

Once the characteristic roots are found, an expression can be determined for the resonant frequencies, f_c, with the following equation:

$$f_c = \frac{\sqrt{\lambda}}{2\pi}\,[\text{Hz}] \tag{11}$$

To convert the corresponding spring-mass system back to the cantilever beam system, the substitution for the spring constants k_1 and k_2 must be made. The following equations give the value of the spring constant for a cantilever beam fixed at one end and free on the other end:

$$k = \frac{3 \cdot E \cdot I}{L^3} \tag{12}$$

$$I = \frac{w \cdot t^3}{12} \tag{13}$$

In Equation 12, *E* represents Young's modulus for the material of the beam, *I* represents the moment of inertia of the beam, and *L* represents the length of the beam. In Equation 13, *w* is the width of the beam and *t* is the thickness of the beam (in the plane that the beam oscillates). A schematic displaying these dimensions is shown in Figure 10.

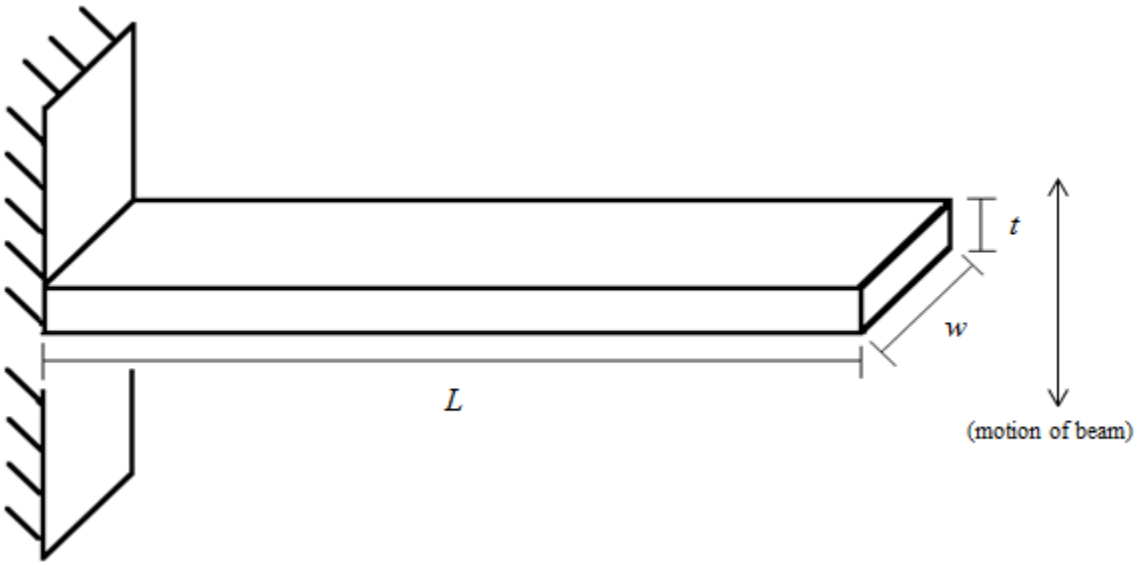

Figure 10: A cantilever beam with its characteristic dimensions.

Once the system's characteristic equations of motion, eigenfrequencies, and eigenvalues are analyzed, the corresponding driving force can be adjusted in order to drive the system to its resonant frequencies. This analysis gives a basic starting point from which to develop the dimensions of the flappers given certain properties of the fluid and materials used in the experiment. A key issue in designing the actual flapper is with guaranteeing that the resulting motion is non-reciprocal. In order to influence the system towards a non-reciprocal nature, one of the joints in the flapper were designed to have a greater range of motion in one direction than the opposing direction. This created a "whip-like" effect in that a greater range of motion in one direction will subsequently cause the successive joint to "snap" like the tail of a whip, and propel the robot forward. Some potential modifications to the flapper in Figure 5 are displayed in Figures 11 and 12.

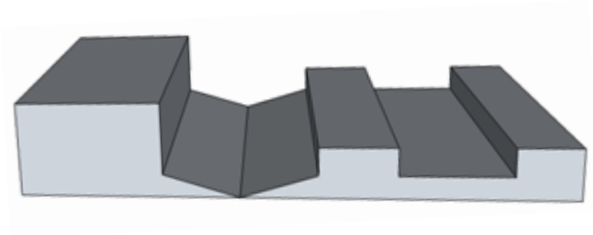

Figure 11: A modified flapper designed to be biased towards non-reciprocal motion.

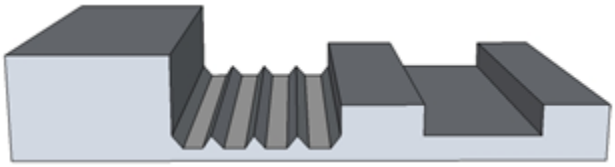

Figure 12: A second modified flapper designed to be biased towards non-reciprocal motion.

Extending the analysis to a system with three masses (to represent the body of the robot, instead of a fixed end for the cantilever beam) follows from the previous analysis, and if the robot body mass is large, it does not change the numerical results significantly. However, once a fluidic environment is introduced, damping within the system will reduce the resonant frequency. This can be modeled within the system by coupling dashpots with a damping factor of *c* to each mass. Such an effect can also be modeled with finite element modeling software such as COMSOL®, which includes a module for coupled fluidic-acoustic interactions.

In order to estimate resonant frequencies, the analysis described in equations (4)-(13) was coded in MATLAB®, using the density and Young's Modulus of polystyrene as a material for the milliscale robot and the parameters of polyMUMPS (a complex, third party microfabrication process) for the eventual microscale robot. The flapper design used in order to estimate the resonant frequencies was the model involving three masses, as displayed in Figure 5. The results were assumed to correlate to the geometry in Figure 4 since the robot body represents the largest mass. The results are summarized in Table 2.

Table 2: A comparison of the theoretical resonant frequencies of the flapper model, calculated from (4)-(13) using dimensions and materials that are typical of the laser cutter for the milliscale and of the polyMUMPS process for the microscale.

Design Iteration	**Resonant Frequency Range**	**Frequency Region**
Milliscale robot (polystyrene)	10 Hz – 1 kHz	Acoustic
Microscale robot (polysilicon)	10 kHz – 1 MHz	Acoustic-Ultrasonic

In order to model the expected motion of the robot, the forces acting on the robot within the fluid must be determined. Figure 13 displays the acoustic forces acting on the equivalent cantilever beam system.

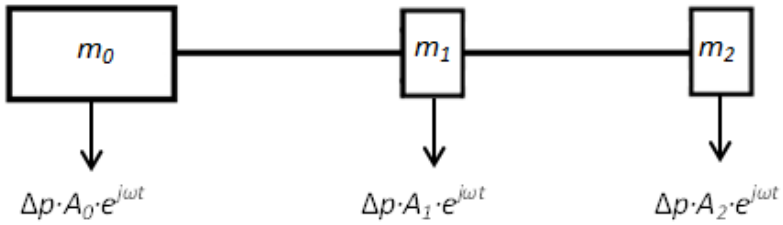

Figure 13: The cantilever beam system displaying the forces acting on it within a fluid.

$$F = \Delta p \cdot A \cdot e^{j\omega t} \tag{14}$$

Equation 14 gives the general formula for the force acting on a mass within the system. The Δp term represents the acoustic pressure on each flap (and its change due to the flapping motion), A represents that cross-sectional area of each mass, and $e^{j\omega t}$ captures the sinusoidal variation of the pressure. Given the previous results from the cantilever beam system, the eigenfrequencies and eigenvectors are known already. Therefore, the cross-sectional area of each mass could be determined from the force required to achieve optimal results as well as the machine limits for fabrication.

In combining all of the theoretical aspects of this project, the project began with the simplest model of the flapping structure that could lead to a more complex structure capable of the project's end goal. From Purcell's work, it is understood that the structure must achieve non-reciprocal motion [12]. By iteratively working through mechanical models, first with a simple beam structure and then transitioning to systems with more complexities, an approach to creating a design with the desired response of non-reciprocal motion in response to acoustic excitation was developed. In the next section, this iterative process is documented.

III. Flapper Design Process

The physical experiments of this work utilized a multi-jointed flapping structure in which non-reciprocal motion was induced in the presence of an acoustic field. The flapping structure needed to couple to the acoustic field in order to provide ample displacement so as to propel the robot structure through the low Reynolds number environment. The flappers and robot structures were fabricated using a 30 W laser cutter from multiple materials, including acrylic, polystyrene, and PETG (polyethylene terephthalate).

The design process involved several iterations, starting at the simplest form of a bending structure, a cantilever beam. As confidence in the COMSOL model was gained through physical testing, the flapper designed gained complexity and eventually led to the design of a satisfactory flapper and robot capable of propulsion in water and lower Reynolds number environments. The iterative process is summarized in Figure 14.

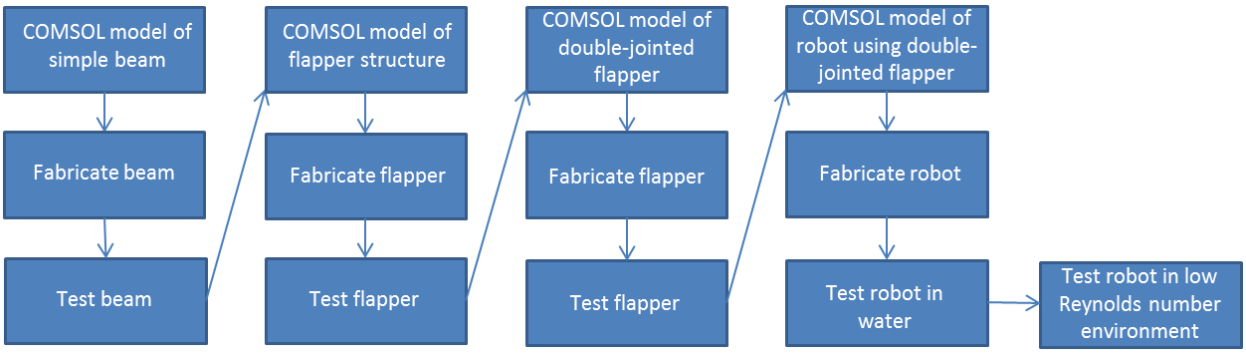

Figure 14: A summary of the iterative design process for the flapper and robot.

IV. COMSOL Modeling

In order to hone in on a flapper design that would react as desired, *i.e.* in a manner tending towards non-reciprocal motion, a 3-D COMSOL model was implemented. The first flapper iteration, shown in Figures 15 and 16, had three masses and two joint sections. The first joint section was designed to be very thin, with the reasoning being that the first joint section would inhibit bending in one direction, but not the opposing direction. Such asymmetry would thus cause non-reciprocal modes for the flapper. The material properties of acrylic, a polymer commonly used in fabrication with the laser cutter, were assigned to the flapper.

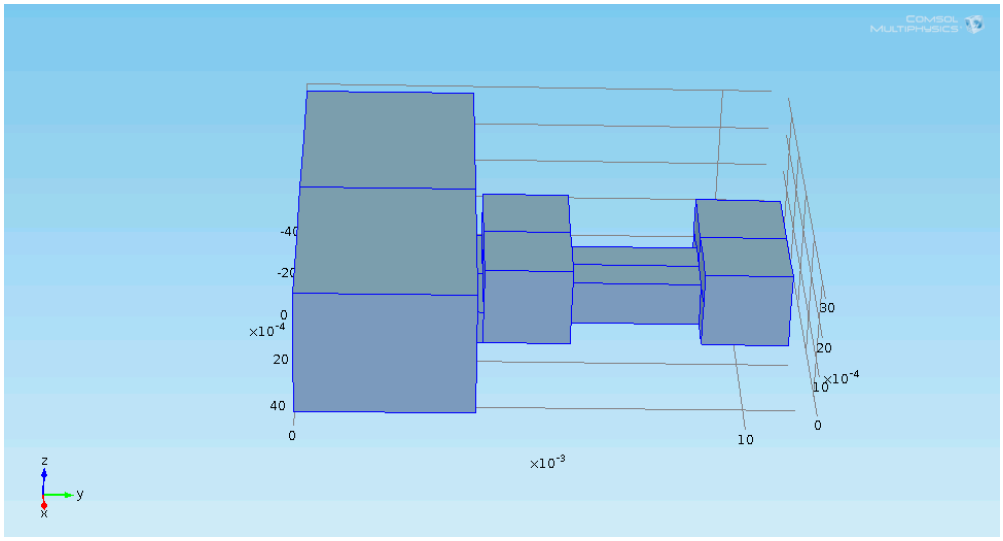

Figure 15: Geometric model implemented in COMSOL of Flapper 0.

Once the flapper geometry was constructed, an eigenfrequency study was run in two separate "environments," one being within an actual fluid and the other being a vacuum. The vacuum model had much shorter computational time (on the order of several minutes as opposed to over an hour) but potentially less realistic results. However, using some theoretical hand calculations, the results of the vacuum model were confirmed to be accurate enough to conduct simulation of the flapper [15].

The results of COMSOL's eigenfrequency study included the eigenfrequencies of the structure as well as their corresponding mode shapes. This was especially useful in determining whether a flapper design could actually result in non-reciprocal motion at a given mode. As shown in Figure 16, the idea of a thin first joint showed promise in that it behaved as predicted: impeding motion in one direction and allowing freedom of motion in the other. This mode is analogous to the asymmetry in a dolphin or whale's kick, which are non-reciprocal movements.

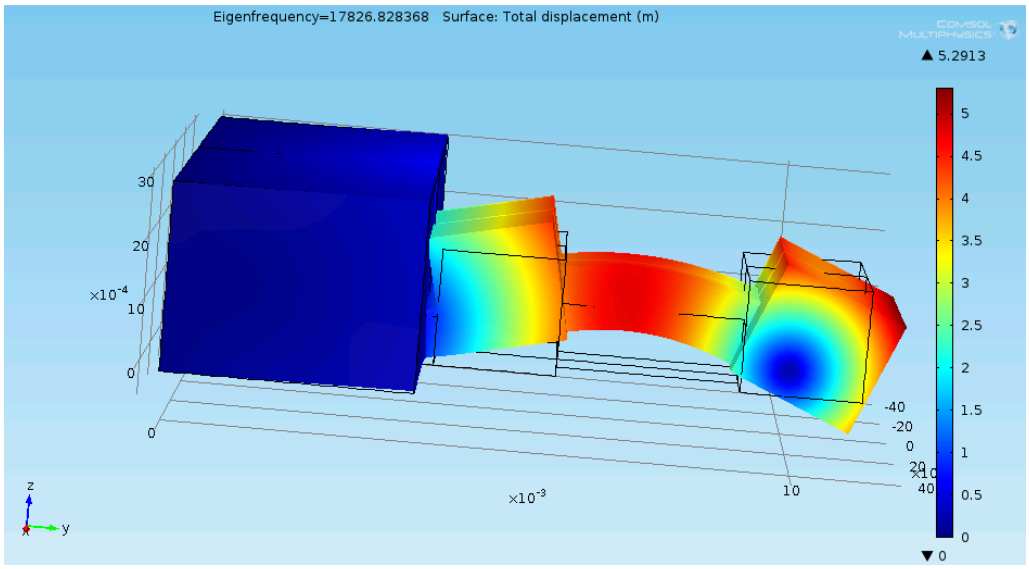

Figure 16: Higher order bending mode of Flapper 0. Note how the thin joint inhibits bending in the displayed motion, but allows freedom of movement in the opposing direction.

Due to issues in testing, specifically that the acrylic used in fabrication was too stiff to achieve meaningful test results, a shift was made from using acrylic to more flexible materials. Styrene and PETG (polyethylene terephthalate) were the two polymers used in developing new COMSOL models due to ease of access in fabrication. Furthermore, these two materials were more flexible and less prone to being overstressed than the acrylic used in fabrication. Thus, a new flapper, Flapper 1, was designed with these materials. Flapper 1 was designed with the intent of creating a simple model whose COMSOL simulations could be easily verified with experimental testing, thus proving the validity of the COMSOL model. Consequently, Flapper 1 was designed with only two masses, one joint, and no grooves or thin joint sections, as shown in Figure 17. The purple sections represent the areas composed of styrene, and the green sections represent acrylic blocks used to tune the resonant frequencies of the flapper.

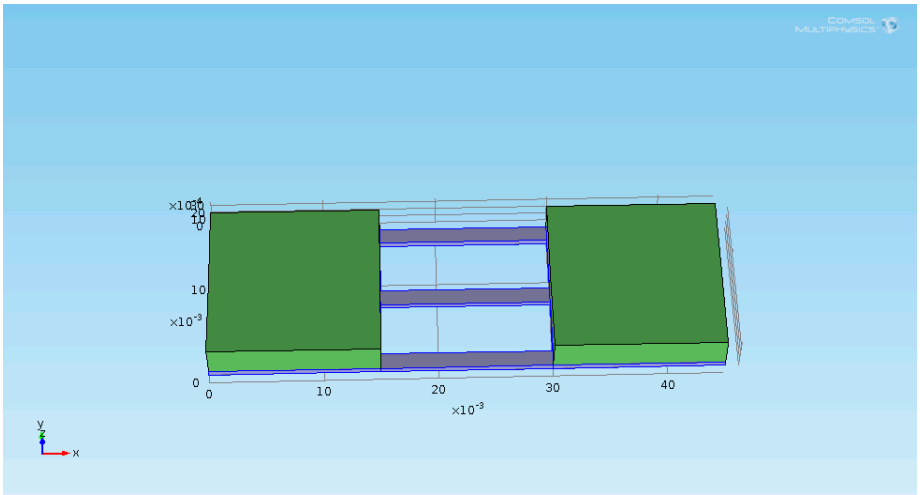

Figure 17: Geometric model of Flapper 1. Green sections are Acrylic, purple sections are Polystyrene.

As with Flapper 0, an eigenfrequency study was run in a vacuum environment. The predicted mode shapes and eigenfrequencies were used to compare with the test results from Flapper 1's fabrication. A higher order mode of Flapper 1 is shown in Figure 18.

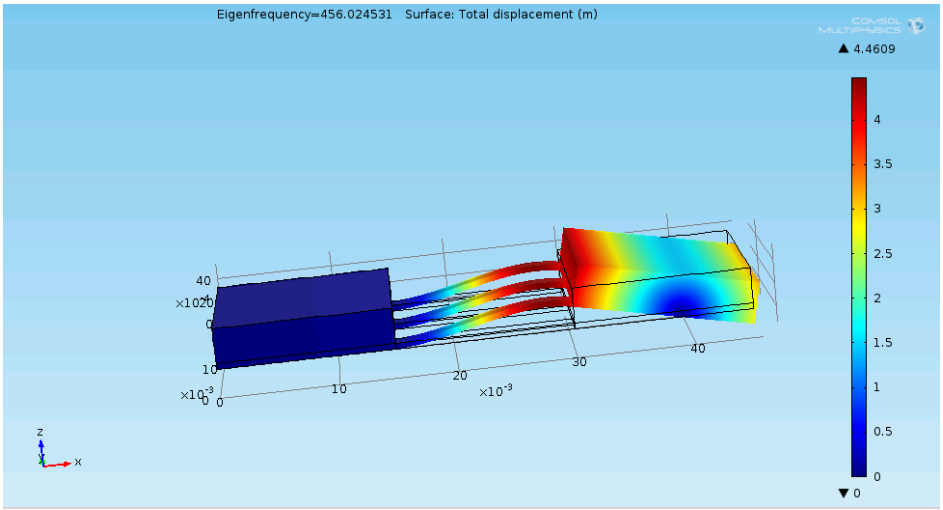

Figure 18: Higher Order bending mode of Flapper 1. In this simulation, the leftmost mass is anchored and the opposing mass is free to move.

Following testing of Flapper 1, our confidence in the COMSOL model's predictions was increased. With simulation and experimental results that matched, the flapper design was modified in order to work towards a structure that would have non-reciprocal modes, like that of Flapper 0. Thus, Flapper 2 was designed with three mass sections, two joint sections, and grooves on the first joint section. The extra mass, joint, and grooves all contribute to the non-reciprocal modes: the mass and joints by giving the structure another degree of freedom (necessary for non-reciprocal motion), and the grooves by influencing the flapper towards an asymmetrical, non-reciprocal pattern. Figure 19 shows the geometric model of Flapper 2; as with Flapper 1, the purple sections are those composed of styrene, and the green sections are acrylic.

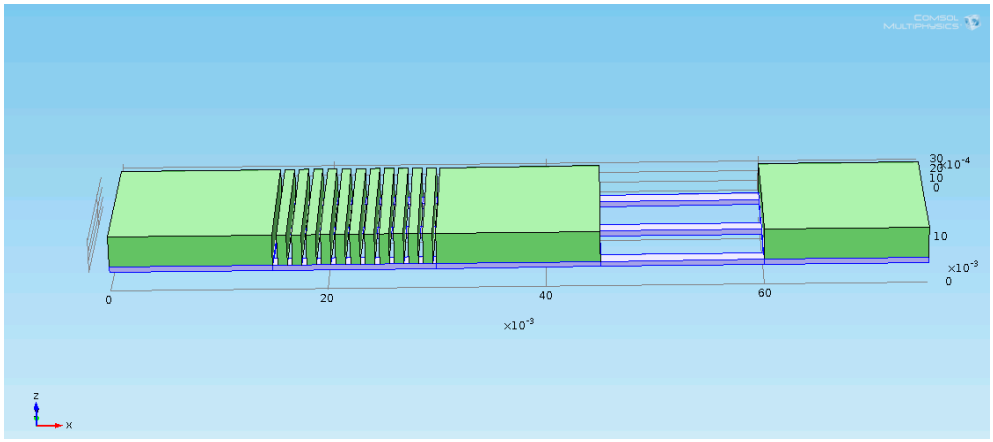

Figure 19: Geometric model of Flapper 2. Note the addition of a third mass and grooved joint section.

Flapper 2 turned out to be the most successful simulation in terms of achieving a structure tending towards non-reciprocal motion. As shown in Figure 20, the eigenfrequency study predicted that Flapper 2 would have several resonant modes that display the type of bending pattern necessary for non-reciprocal motion. If the mode shape displayed in Figure 20 was filmed in time, one would notice that the first joint section wouldn't be able to bend as freely in the opposing direction, while the second joint section would flex in the opposite manner and create a "kicking" motion analogous to a dolphin's kick. Such motion is classified as non-reciprocal and would lend itself towards propulsion in a low Reynolds number environment.

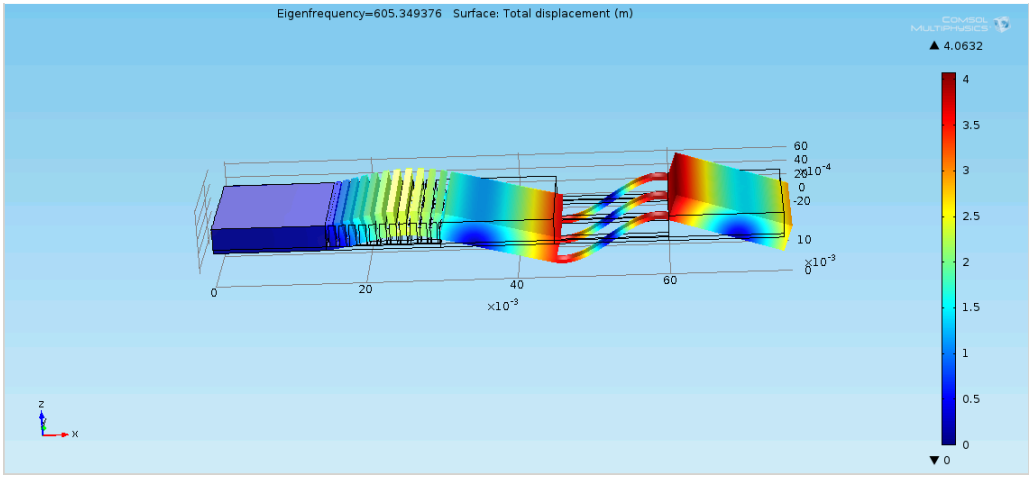

Figure 20: Higher order bending mode of Flapper 2. Note how the grooved section allows uninhibited bending in the displayed motion, yet inhibits bending in the opposing direction.

In addition to the bending modes predicted for each flapper structure, COMSOL also predicted the presence of torsional, or twisting, modes, displayed in Figures 21 and 22. Torsional modes are those where the structure rotates about a central axis, unlike bending modes, where the structure flexes or extends as a result of a load applied perpendicularly to the longitudinal axis of the structure. All structures, such as the above flappers, which are assumed to behave like cantilever beams, will have modes such as these torsional modes. While these modes could have been cause for concern (for sometimes causing a structure to fail), the modes predicted for the flappers did not pose a problem. Rather, the flappers were simply designed so that the eigenfrequencies that cause bending modes are not too close to the torsional modes. This ensured

that when excited at a frequency designed for bending, the flapper was excited to a hybrid bending-twisting mode.

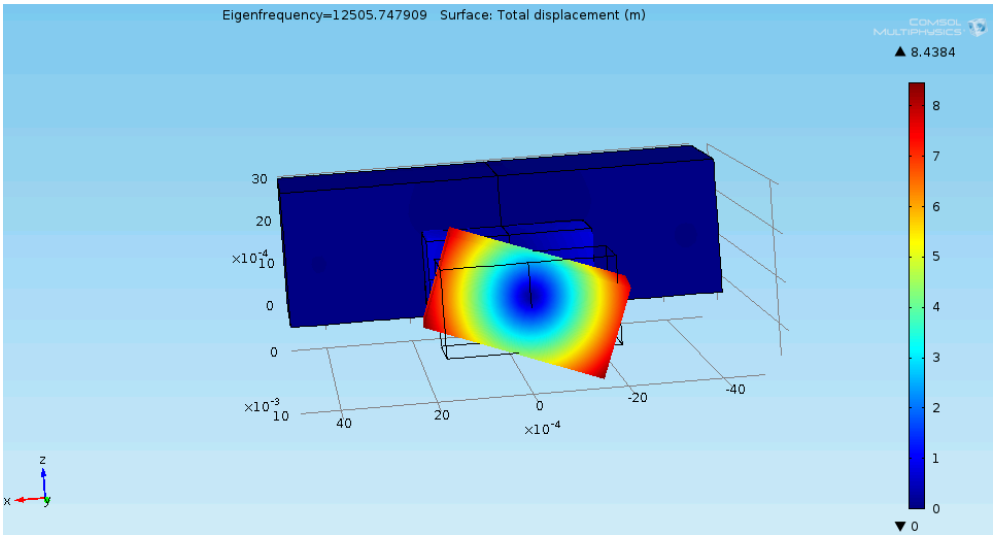

Figure 21: A torsional (twisting) mode of Flapper 0. Note that it is characterized by rotation about a central axis.

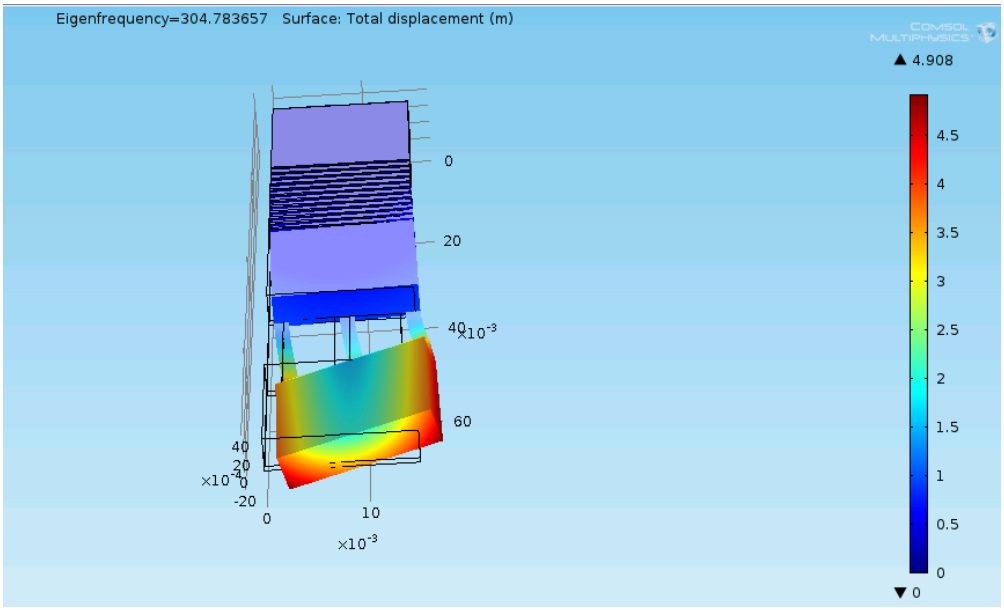

Figure 22: A torsional (twisting) mode of Flapper 2.

V. Fabrication

The flappers simulated in COMSOL were fabricated using a VLS 3.50 30 Watt laser cutter. The laser cutter has a resolution of approximately 25 μm and can cut a wide variety of polymers and other materials. Due to the laser cutter being on site and having average runtimes of 1-2 minutes, turnaround for flapper fabrication was very quick. This allowed for greater variance in the flapper design and testing.

Initially, acrylic was the only material used in fabrication. Acrylic was chosen because it is a common material used with the laser cutter. The flapper design was initially tuned for specific resonant frequencies with acrylic in mind as the sole material. However, acrylic turned out to be an undesirable choice due to its fairly stiff nature (resulting from thick samples) and poor flexural strength (flappers would break when dropped or driven too severely). Furthermore, when testing flappers fabricated solely with acrylic, the mode shapes and resonant frequencies were difficult to image and measure since the flapper didn't achieve significant displacement.

Due to acrylic's shortcomings, particularly in the inability to obtain meaningful test results, flapper fabrication was shifted to the materials polystyrene and PETG. Both materials have somewhat similar properties to acrylic [16], but the actual sheets of styrene and PETG available were both much thinner than the acrylic sheets used for fabrication. This in turn made them functionally more flexible; in other words, the effective spring constant, *k*, with these materials was much lower, as shown in Table 3. In fabricating the flapper with these new materials, the joint sections were composed of the more flexible material (styrene or PETG) and acrylic blocks were bonded (using JB Weld epoxy®) onto the square mass sections. The flexible flappers were much more successful in that the resonant frequencies were much more easily measured and the mode shapes were captured with the high-speed camera. This design also had the advantage that the acrylic mass blocks allowed for easier tuning of resonant frequencies of the flapper.

Table 3: Analysis of spring constant k for constant dimensions w and l, and other dimensions based on physical measurements of samples of acrylic, styrene, and PETG on hand for fabrication [16].

Material	**Young's Modulus [Pa]**	**Inertia ($N*m^2$)**	**Width (m)**	**Thickness (m)**	**Length (m)**	**Spring Constant, *k* (N/m)**
Acrylic	3.20×10^{9}	2.25×10^{-11}	1.50×10^{-2}	2.62×10^{-3}	7.50×10^{-2}	511.57
Styrene	3.50×10^{9}	1.76×10^{-13}	1.50×10^{-2}	5.20×10^{-4}	7.50×10^{-2}	4.37
PETG	3.00×10^{9}	2.70×10^{-13}	1.50×10^{-2}	6.00×10^{-4}	7.50×10^{-2}	5.76

VI. Flapper Testing

Initial tests of the flapper consisted of a mechanical shaker as the excitation source and a fiber optic displacement sensor in order to measure the response of the flapper. This system is shown in Figure 23.

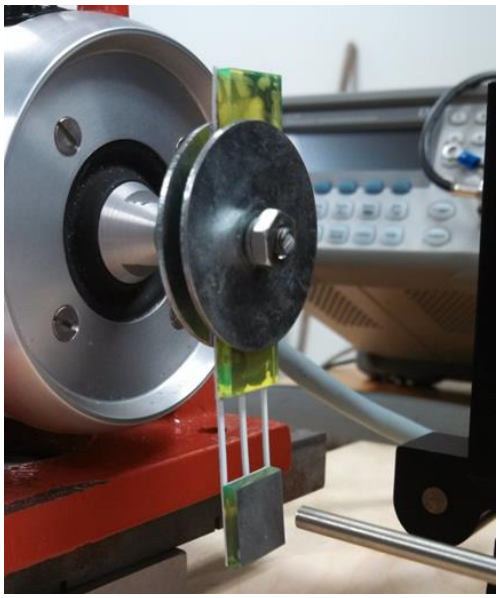

Figure 23: The mechanical shaker with Flapper 1 attached to the shaker structure. The fiber optic sensor is in the bottom right corner.

In order to determine the response of the flapper, the fiber optic sensor was calibrated so that the input signal could be swept over a range of frequencies and the sensor would subsequently measure the displacement of the unfixed end of the flapper. The sensor works by measuring the intensity of reflected light off of the displaced surface. One issue with the flappers was that the acrylic mass sections did not initially reflect enough light to obtain a good response signal with the fiber optic sensor. Thus, the flapper ends had to be modified using lustrous silver paint, as shown in Figure 24. This paint had negligible effects upon the flapper's motion and bending properties since only a small amount of paint was added.

Furthermore, since the connections from the fiber optic sensor to the oscilloscope were not ideal, noise was introduced to the output signal. Consequently, in order to obtain meaningful results, the output signal was filtered using a Dual 1569-7 10^{th} order low pass filter [17].

Figure 25 shows a block diagram of the experimental setup.

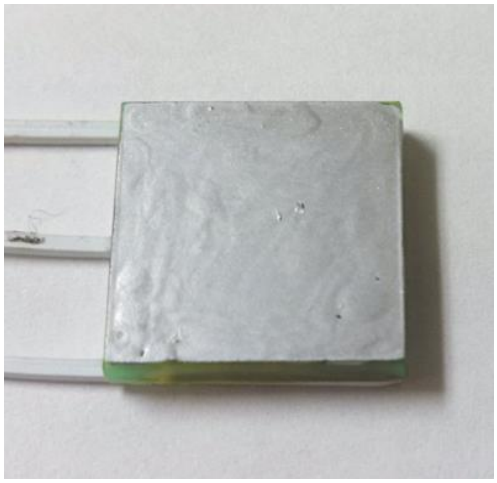

Figure 24: Silver paint used to help aid the fiber optic sensor in detecting flapper displacement.

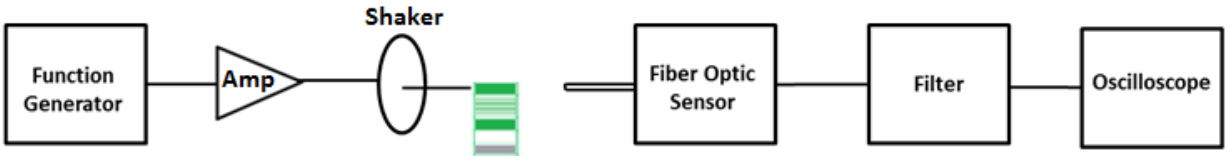

Figure 25: Block Diagram of shaker test setup

A. Flapper 0

Initial tests of Flapper 0, shown in Figure 26, using the mechanical shaker and fiber optic sensor indicated a presence of eigenmodes, yet not necessarily with high fidelity to the predictions of the corresponding COMSOL model. Furthermore, due to the fact that the flapper was fairly small (largest dimension ~ 15 mm) and that the acrylic used in fabrication was quite stiff, the fiber optic sensor had issues in detecting displacement of the flapper, and the mode shapes could not be filmed using the high speed camera. Despite this, several eigenfrequencies were successfully measured, indicating that the there was some positive correlation between the accuracy of the COMSOL model and the test results. Ultimately, the issues highlighted above led to a change in design, specifically using more flexible materials as well as increasing the size scale in order to allow for easier mode shape detection.

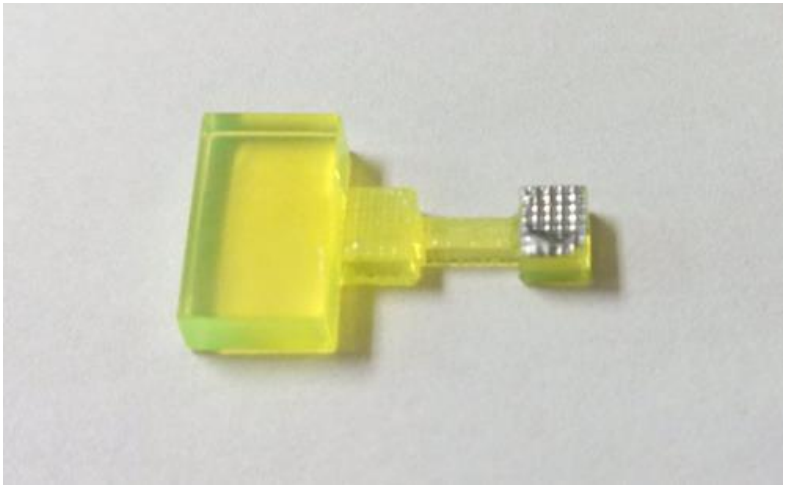

Figure 26: Flapper 0 after fabrication. Green sections are acrylic and silver finish is paint to aid the fiber optic sensor. Flapper dimensions approximately 15 mm long and 5 mm wide.

B. Flapper 1

The shaker test results from Flapper 1, shown in Figure 27, indicated close agreement with the COMSOL predictions. Four resonant frequencies, ranging from 25 Hz to 310 Hz, were detected with the fiber optic sensor. These results are displayed in Figures 28-30 and Table 4. The reason for the different graphs and axes scales is due to the fact that the input signal needed to be changed for each range of frequencies. As the signal input to the shaker reached higher frequencies, the input voltage was increased in order to see a noticeable output from the fiber optic sensor.

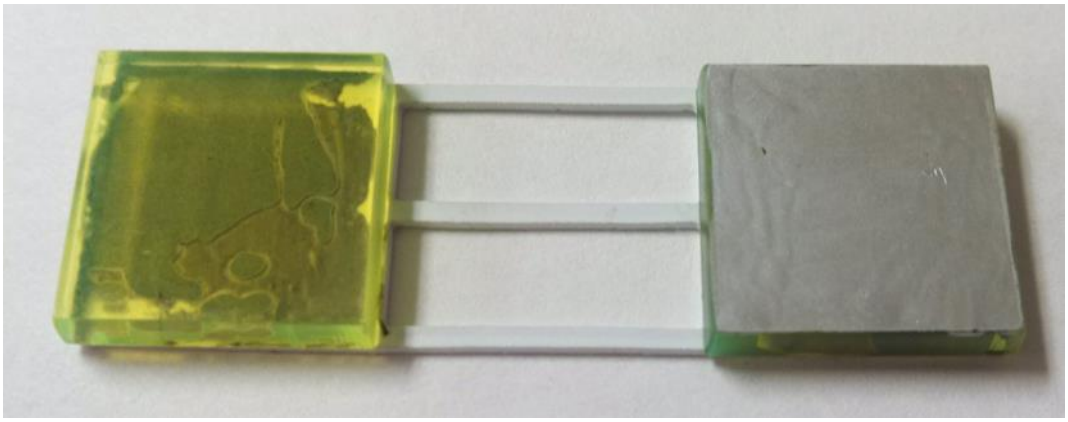

Figure 27: Flapper 1 after fabrication. Green sections are acrylic, white sections are styrene, and silver finish is paint to aid the fiber optic sensor. Flapper dimensions are approximately 45 mm long and 5 mm wide.

The first mode for Flapper 1, located at 25 Hz, indicates a bending mode (Figure 28). Since the peak voltage output is much greater than the other local output voltages, a bending mode makes sense. This result also matches with the COMSOL prediction that the first mode for Flapper 1 would be a bending mode. Table 4 has a comparison between expected eigenfrequencies and mode shapes and actual eigenfrequencies and mode shapes.

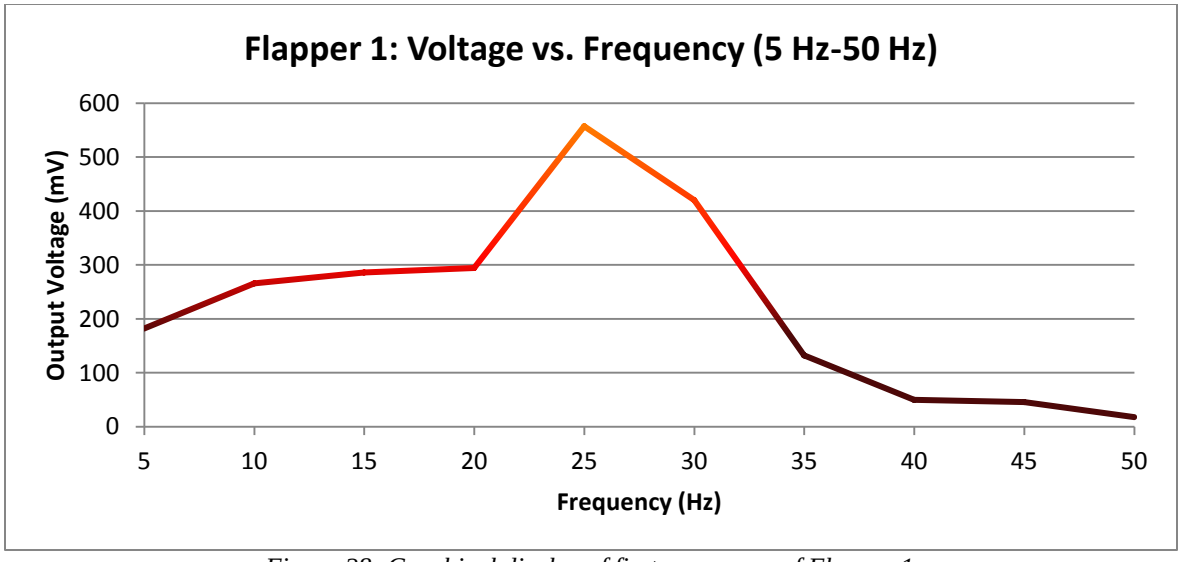

Figure 28: Graphical display of first resonance of Flapper 1.

The second and third modes for Flapper 1 were predicted to be twisting modes by COMSOL. The shaker tests seem to confirm that the second and third modes did not exhibit as large of a relative output voltage peak as the first resonant mode, as illustrated in Figure 29. A partial explanation for this is due to the placement of the fiber optic sensor. Since the fiber optic sensor only measures the displacement at a very small point on the flapper, the twisting modes would accordingly be more difficult to measure than the bending modes.

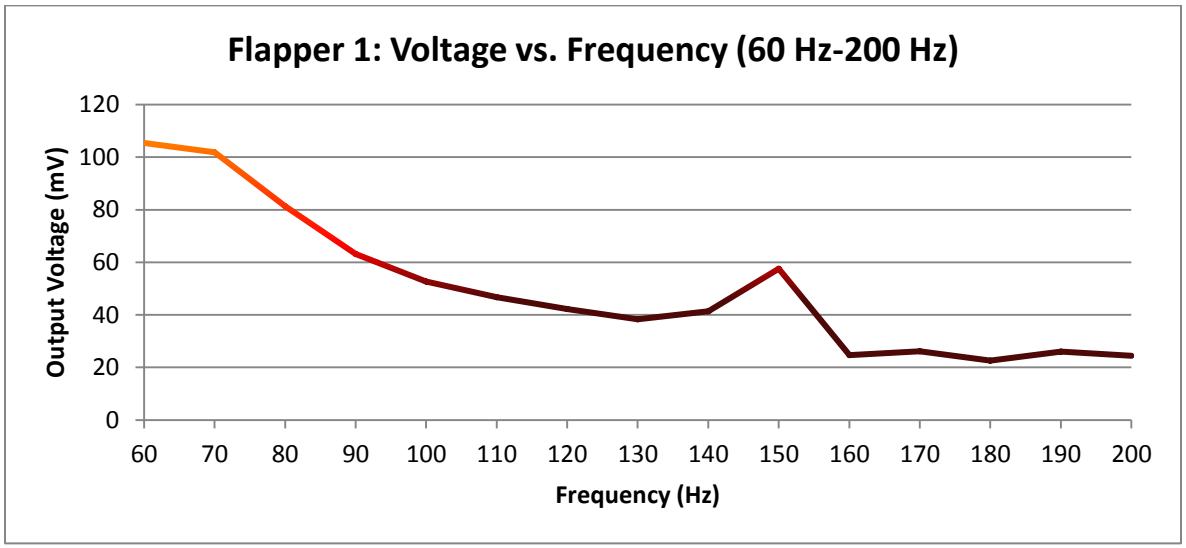

Figure 29: Graphical display of second and third resonant peaks of Flapper 1.

The fourth eigenfrequency of Flapper 1 was predicted to be a bending mode in the COMSOL simulation. This prediction was confirmed by the fiber optic sensor. Similar to the first mode, the peak output voltage was significantly larger than the local output voltages, indicative of a bending mode, as displayed in Figure 30.

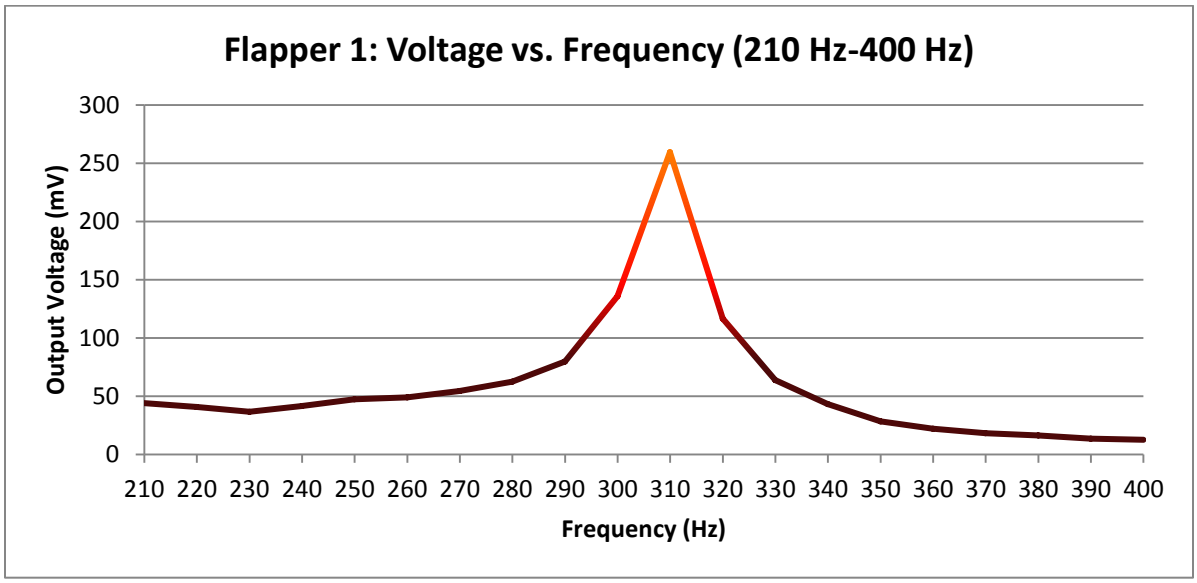

Figure 30: Graphical display of fourth resonance frequency of Flapper 1.

Table 4 displays an interesting result in addition to the comparison of expected vs. actual eigenfrequencies and mode shapes. The column labeled "Ratio to First Mode" displays the ratio of each eigenfrequency to the initial mode, both in the expected and actual columns. The differences between the actual and expected ratios for corresponding modes are quite similar, meaning that the relative spacing between modes matches up quite well between the COMSOL model and shaker test results. The biggest discrepancy was with the third mode, most likely due to the fact that this mode was a twisting mode. Since the fiber optic sensor only measured the flapper's displacement at one point on the flapper, the twisting modes were harder to measure accurately. However, the bending modes were predicted with fairly good accuracy. This finding, along with the verification that the mode shapes match with the predictions, gave credibility to the COMSOL model for Flapper 1.

Table 4: Summary of shaker test results for Flapper 1.

COMSOL Predictions			**Measured Results**		
Expected Eigenfrequencies (Hz)	**Ratio to First Mode**	**Expected Mode Shape**	**Actual Eigenfrequencies (Hz)**	**Ratio to First Mode**	**Actual Mode Shape**
36.40	1.0	Bending	25	1.0	Bending
202.59	6.0	Twisting	150	5.6	Twisting
393.59	7.6	Twisting	190	10.8	Twisting
456.02	12.4	Bending	310	12.5	Bending

Figures 31 and 32 display several still images captured from high speed video of the flapper excited at different modes. The high speed video also helped confirm the actual mode shapes present at each eigenfrequency.

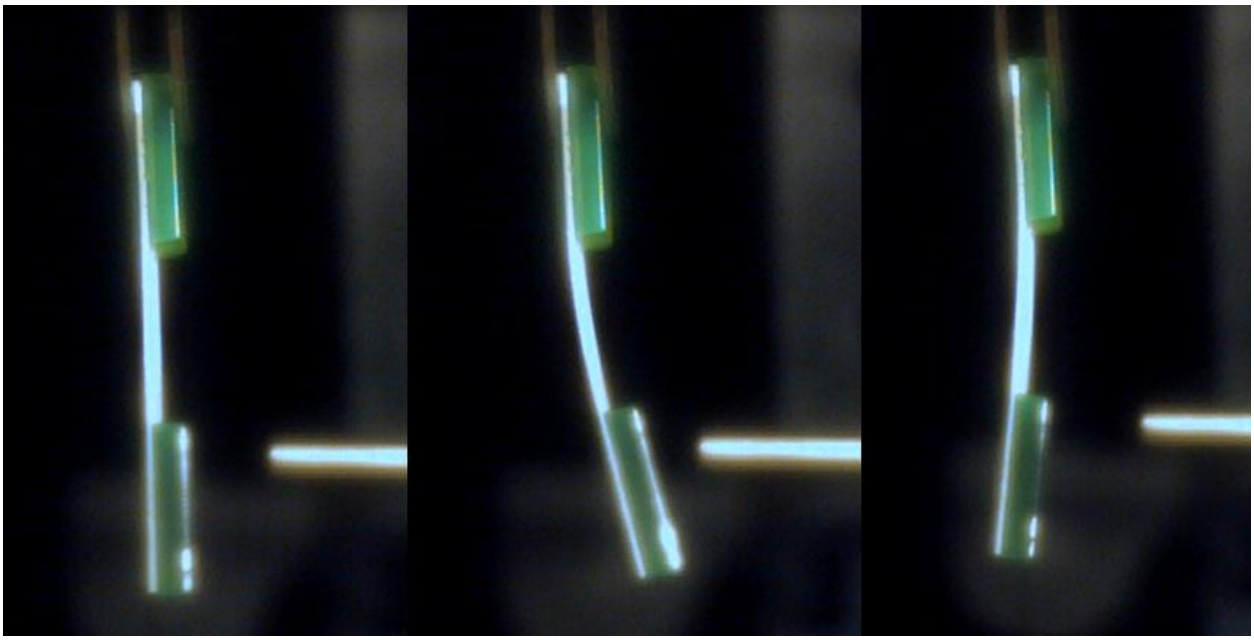

Figure 31: Still images taken from the high speed video of the 25 Hz bending mode.

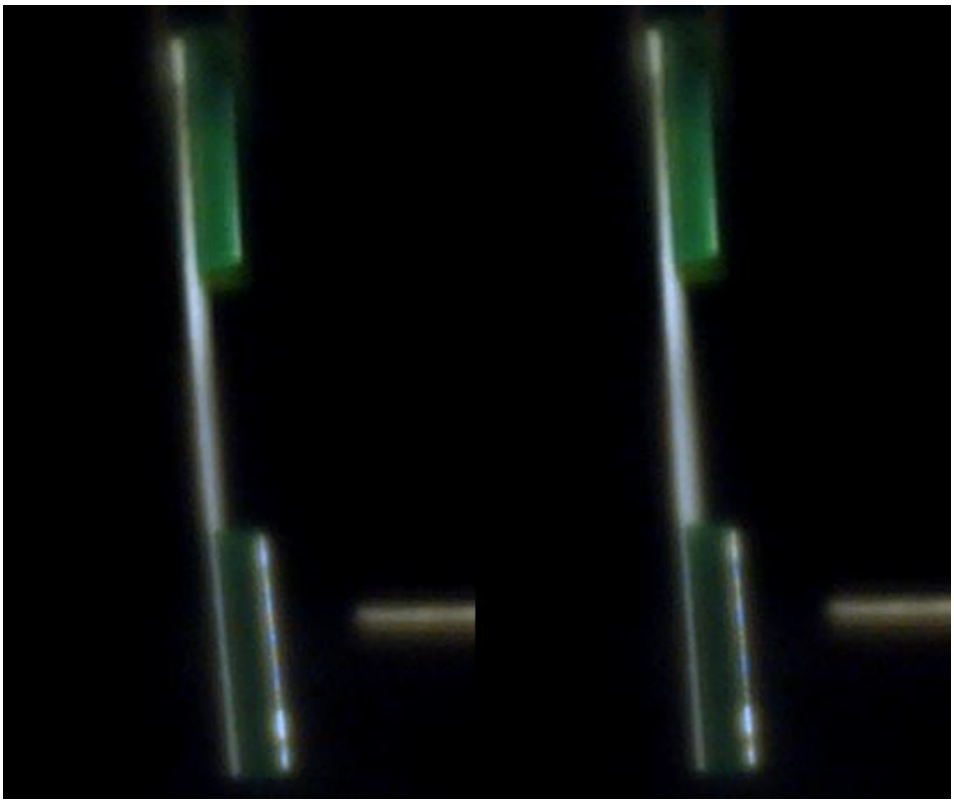

Figure 32: Still images from the 150 Hz mode. Note how the middle joint appears to grow thicker in the rightmost image-this is due to the twisting nature of the mode.

C. Flapper 2

As with Flapper 1, the shaker test results from Flapper 2, shown in Figure 33, indicated close agreement with the COMSOL predictions. Four eigenfrequencies, ranging from 15 Hz to 650 Hz, were detected with the fiber optic sensor. These results are displayed in Figures 34-37 and Table 5. The first two modes were bending modes, the middle two were torsional modes, and the last two were bending modes. Three out of the four bending modes (modes 2, 3, and 4) were characterized by "double bend" shapes as predicted in the COMSOL model (see Figure 20).

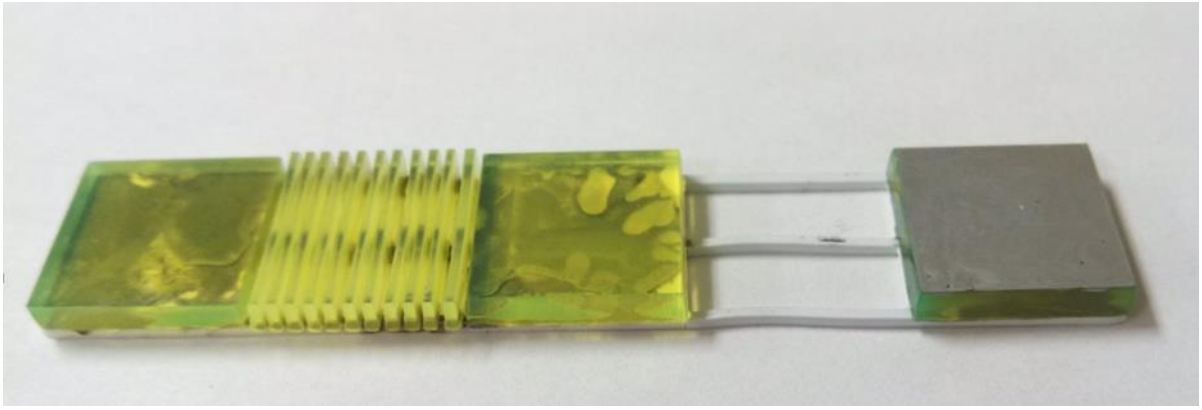

Figure 33: Flapper 2 after fabrication. Green sections are acrylic, white sections are styrene, and silver finish is paint to aid the fiber optic sensor. Dimensions are approximately 75 mm long and 5 mm wide.

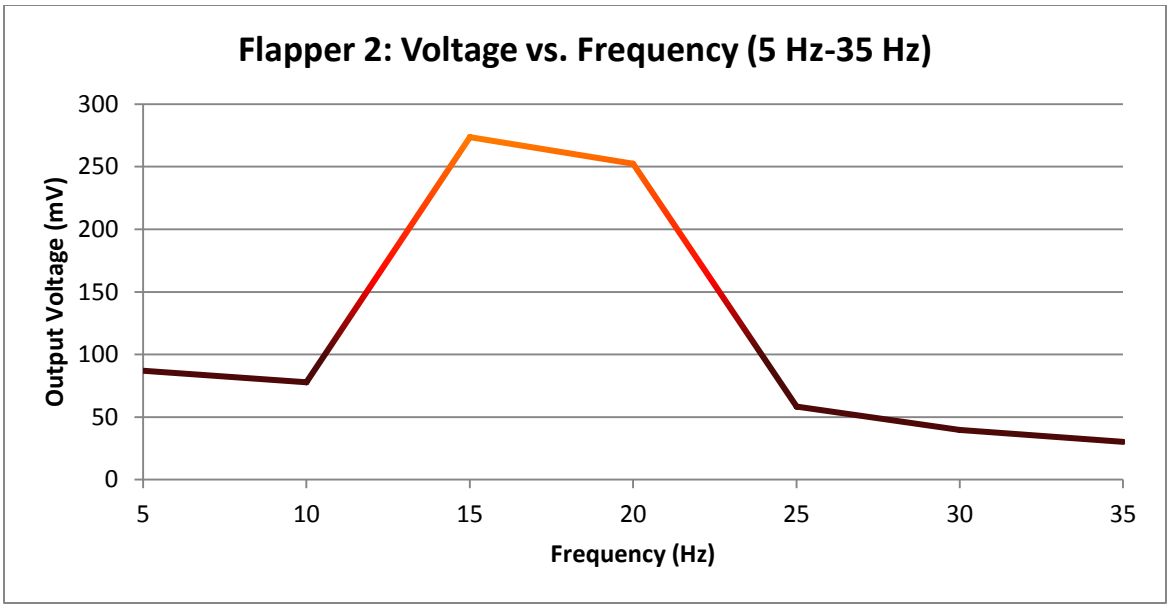

Figure 34: Graphical display of the first resonance peak of Flapper 2. The first mode is a bending mode ***not*** *characterized by a double bend shape.*

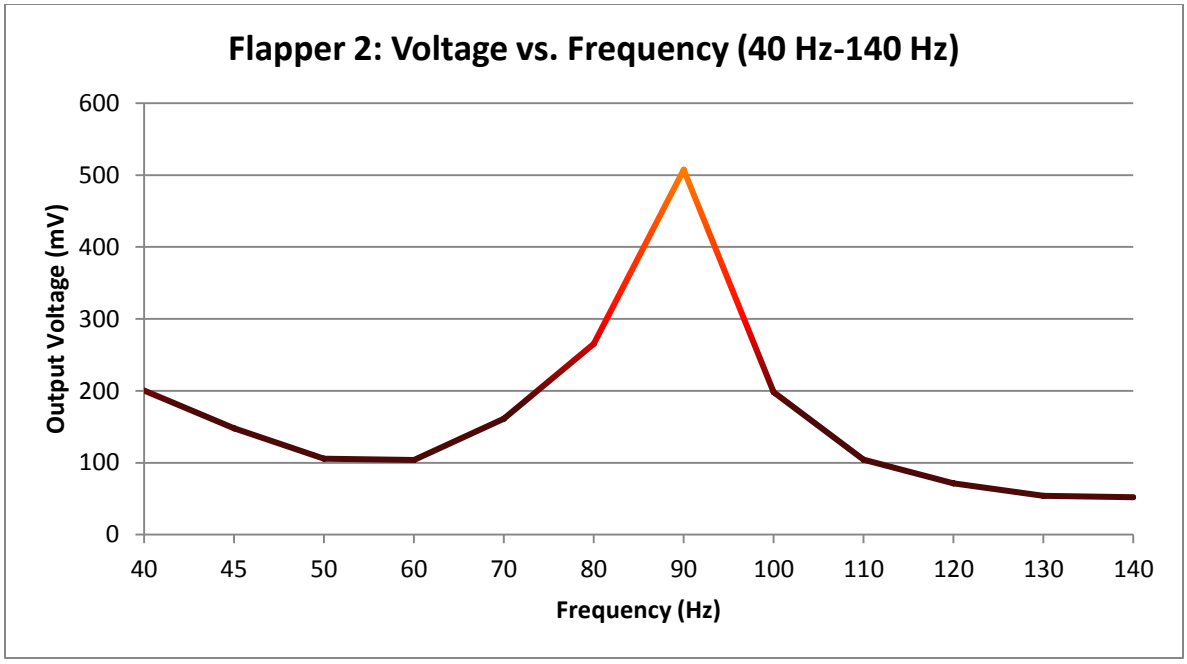

Figure 35: Graphical display of the second resonance peak of Flapper 2. The second mode is bending mode, one of the double bend shapes similar to Figure 20.

The third and fourth modes for Flapper 2 were predicted to be twisting modes by COMSOL. The shaker tests seem to confirm that, as the second and third modes did not exhibit as large of a relative output voltage peak as the first resonant mode, as displayed in Figure 36. A partial explanation for this is due to the placement of the fiber optic sensor. Since the fiber optic sensor only measures the displacement at a very small point on the flapper, the torsional modes would accordingly be more difficult to measure than the bending modes.

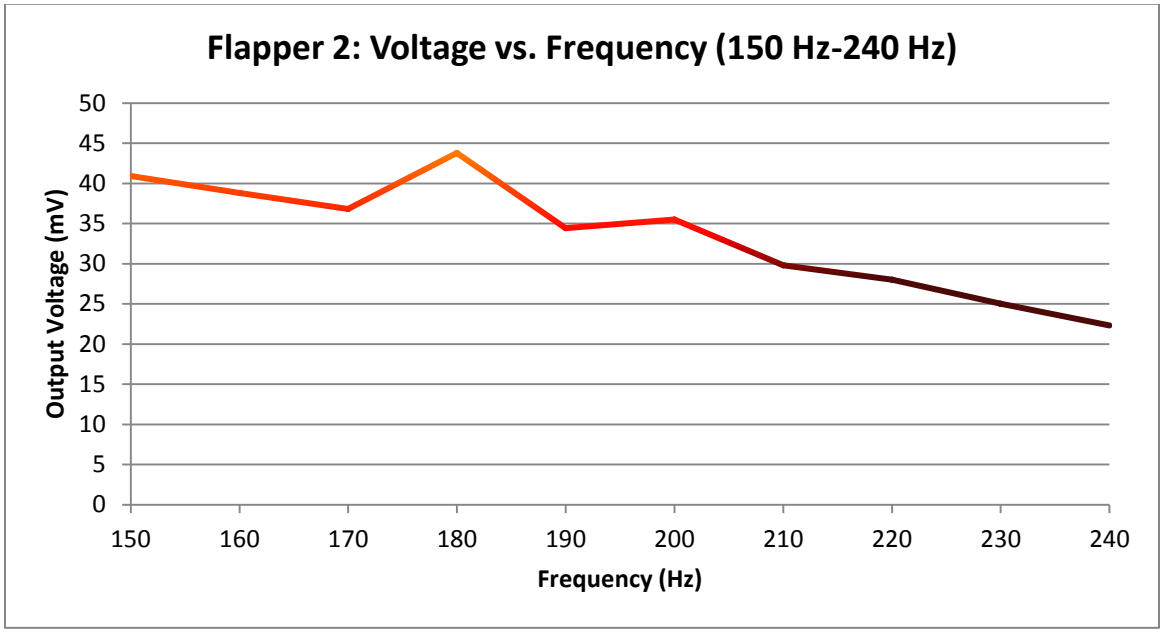

Figure 36: Graphical display of third and fourth resonant peaks of Flapper 2. Both modes are twisting modes.

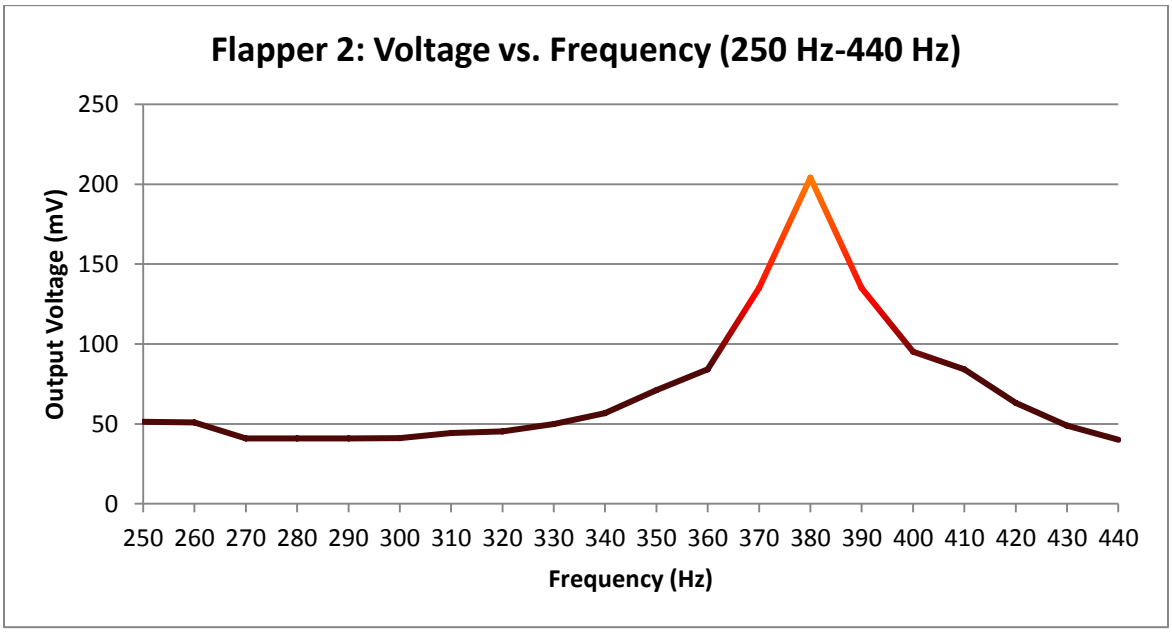

Figure 37: Graphical display of fifth resonant peak of Flapper 2. The fifth mode is characterized by a double bending mode shape.

The sixth eigenfrequency was not graphed due to a difficulty in detection of the mode. The oscilloscope had a tough time picking up the output voltage signal, most likely due to two resonance modes being close to each other. The output voltage signal appeared to have two distinct frequencies, as if two sine waves of similar amplitude had been summed. However, the high speed camera confirms that Flapper 2 had an eigenfrequency at approximately 650 Hz.

As with Flapper 1, the eigenfrequencies and mode shapes matched up quite well with the COMSOL predictions, shown below in Table 5. In fact, some of the eigenfrequencies were less than 10 Hz away from the actual predictions. Furthermore, the ratio to the first mode once again showed that the actual eigenfrequencies were at the spacing between successive modes that the COMSOL model predicted. Once again, the biggest discrepancy was with a twisting mode, the fourth mode, due to the fiber optic sensor's limitations. Finally, the mode shapes of Flapper 2 were confirmed to match the COMSOL predictions through high speed video captures. Ultimately, the results of the shaker tests gave us great confidence in trusting the validity of the COMSOL model.

Table 5: Summary of shaker test results of Flapper 2.

COMSOL Predictions			**Measured Results**		
Expected Eigenfrequencies (Hz)	**Ratio to First Mode**	**Expected Mode Shape**	**Actual Eigenfrequencies (Hz)**	**Ratio to First Mode**	**Actual Mode Shape**
14.39	1.0	Bending	15	1.0	Bending
95.17	6.0	Bending (double bend)	90	6.6	Bending (double bend)
189.75	12.0	Twisting	180	13.2	Twisting
304.78	13.3	Twisting	200	21.2	Twisting
331.03	25.3	Bending (double bend)	380	23.0	Bending (double bend)
605.35	43.3	Bending (double bend)	650	42.1	Bending (double bend)

High speed video was also used to confirm the actual mode shapes present at each eigenfrequency for Flapper 2. Figures 38 and 39 display still images from the 15 Hz mode and 90 Hz mode for Flapper 2.

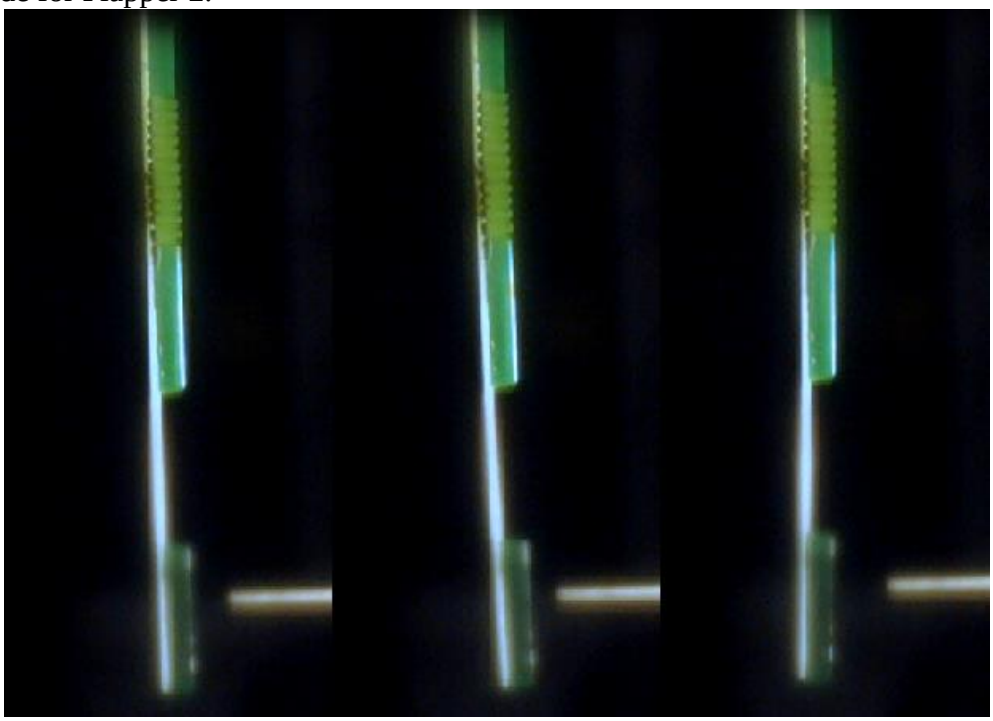

Figure 38: Still images of the 15 Hz mode for Flapper 2. Note the change in distance from the fiber optic sensor to the third mass, indicating a bending mode.

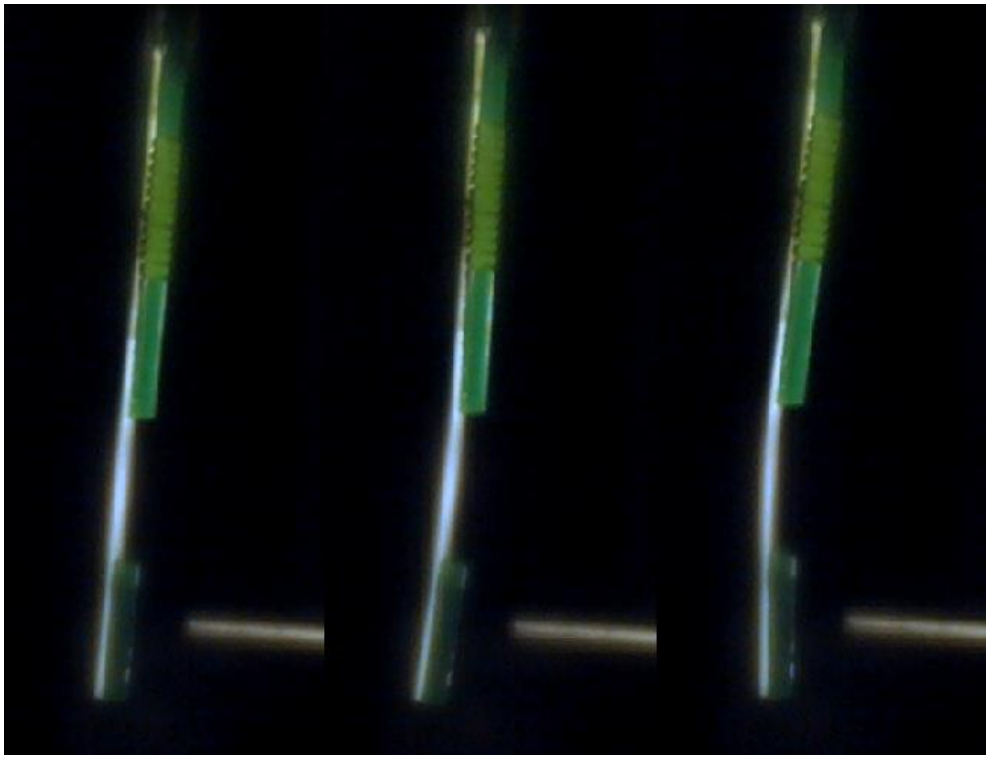

Figure 39: Still images of the 90 Hz mode for Flapper 2. Note the double-jointed bending of the flapper.

VII. Robot Testing

Following confirmation of the expected and actual behavior of the flapper, a robot incorporating the double-jointed flapper was designed to facilitate propulsion while submerged. A similar process was followed with the robot design, fabrication, and testing as with the flappers.

A. Swimmer Design and Fabrication

The swimming robot is shown in Figure 40. The robot was designed so that the large body section would allow for greater coupling to the acoustic field while also allowing for forward displacement in a fluid. The robot was modeled in COMSOL to determine a rough estimate of the resonance modes as well as its behavior over several periods of motion. It was fabricated in the same fashion as the flappers, with the materials PETG and acrylic using a 30 Watt laser cutter.

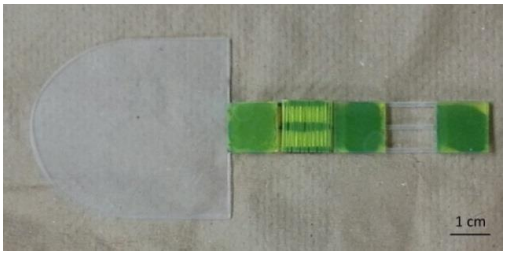

Figure 40: The swimming robot, consisting of a styrene head with the double-jointed flapper attached as a tail.

B. Fluidic Environment Testing

Following modeling and fabrication, the robot was tested within a fluidic environment. Water was used for initial testing. The test setup involved a 16”x16”x10” tank surrounded by acoustic damping foam and filled with the desired test fluid, and a 30 W underwater speaker in the center of the tank (Figure 41). The input was controlled by a function generator and amplifier. In order to capture the motion of the robot, a camera was placed directly above the speaker. In order to constrain the vertical position of the robot, since neutral buoyancy was not attained in water, a horizontal track was set up using thin lines to support it above the speaker. All fluidic tests were conducted at room temperature with no outside controller to constrain the temperature.

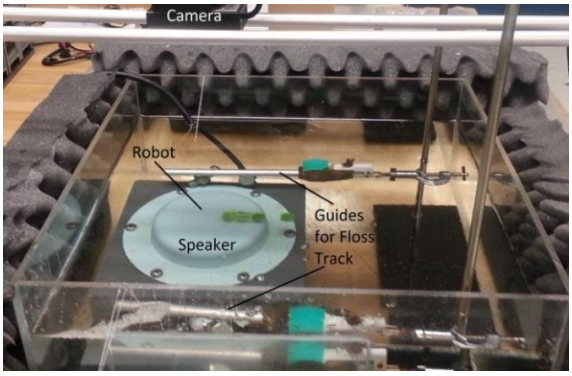

Figure 41: The fluidic environment test setup consisted of a tank with an underwater speaker attached to a function generator via an audio amplifier. A camera is suspended above the tank. A horizontal track was set up using floss to maintain the vertical position.

Following successful video capture, the data was analyzed using MATLAB®. The images captured were processed frame by frame in order to track the centroid (Figure 42) and orientation of the robot and thus, its movement over time. This analysis allowed for the calculation of the forward velocity of the robot through the fluid.

Figure 42: Comparison of an actual video frame and the same frame processed in MATLAB to compute the centroid of the robot in order to track its position over time.

C. Swim Test Results

The robot was observed to move forward at the resonance frequency for the flapper. Figure 43 shows the position of the centroid in pixels for a 173 Hz excitation over roughly a 20 s time period, and Figure 44 shows the frame-to-frame forward velocity. The motion of the robot in response to the 173 Hz source is not perfectly linear but achieves clear forward motion at an average velocity of approximately 2.5 mm/s.

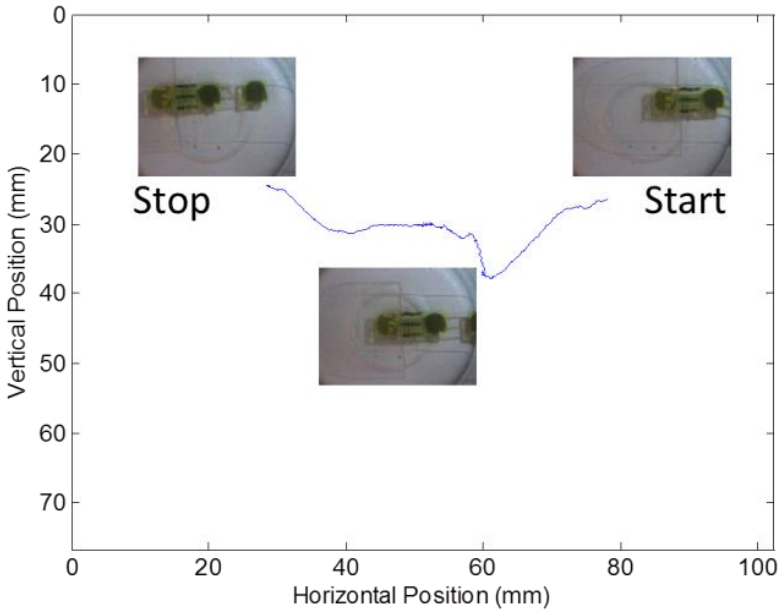

Figure 43: Robot position (in mm) at 173 Hz, showing its forward travel (from right-to-left) with corresponding frames overlaid.

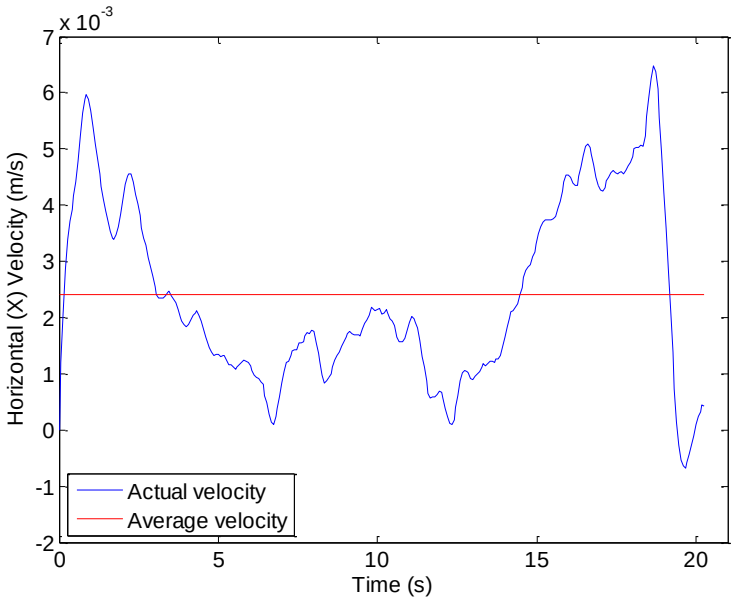

Figure 44: Robot forward velocity as function of time for excitation at 173 Hz. The average is 2.5mm/s.

Figure 45 demonstrates the frequency selectivity of the mechanism. Like the flapper models, the robot has close agreement with COMSOL in terms of resonance mode spacing. The COMSOL model predicted eigenfrequencies approximately 115 Hz and 140 Hz, and the robot responds to inputs of roughly 140 Hz and 173 Hz. These discrepancies are most likely due to the fact that the COMSOL model was simulated within a vacuum, and the actual robot testing occurred within a fluidic environment. Furthermore, the lower mode was predicted to have some twisting elements as well as bending motion while the 173 Hz mode was predicted to be a purely bending mode. This is corroborated by the different average velocities, with the twisting-bending hybrid mode having a smaller velocity than the pure bending mode.

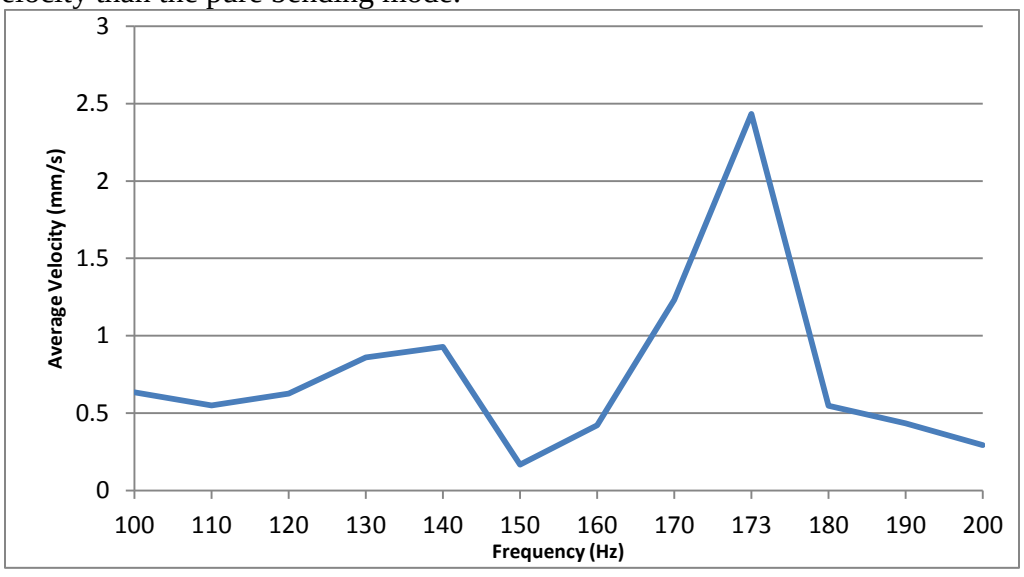

Figure 45: Robot forward velocity as function of excitation frequency.

VIII. Low Reynolds Number Testing

In order to achieve a fluidic environment mimicking the microscale, the robot was then tested within a more viscous fluid. Glycerine was combined with water in order to achieve a viscosity in between the nominal values for water (8.90×10^{-4} Pa·s) and glycerine (0.950 Pa·s). The viscosity was measured using a Brookfield rotational viscometer, using an average of three viscosity readings at three different viscometer rpm settings. Table 6 shows a comparison of the fluidic environment regimes, ordered by decreasing Reynolds number, and the average velocity achieved by the robot in those conditions.

Table 6: Comparison of Fluidic Environment Conditions[2] and Reynolds Number.

Fluid	Density (kg/m^3)	Velocity (mm/s)	Length (mm)	Viscosity (Pa·s)	Reynolds Number
Water	1000	2.5	130	8.9×10^{-4}	365
Water-Glycerine (~60% glycerine)	1170	2.4	130	7.6×10^{-3}	48.0
Water-Glycerine	1170	2.3	130	2.1×10^{-2}	16.7
Water-Glycerine	1170	1.8	130	2.4×10^{-2}	7.6
Water-Glycerine (~80% glycerine)	1170	1.5	65	2.6×10^{-2}	4.4

Figure 46 shows the actual motion of the robot when excited at 186 Hz submerged within the water-glycerine solution. As indicated by the motion of the robot, as well as in Figure 47 (velocity vs. time), the robot achieved the most direct propulsion when over the center of the speaker, as indicated by the straight section of motion and acceleration over this part of the speaker. This is due most likely to the acoustic field coupling to the robot most strongly, since the acoustic field was strongest in that area in addition to the robot having its largest surface area presented to the speaker.

[2] Readings for temperature and density taken at 21° C

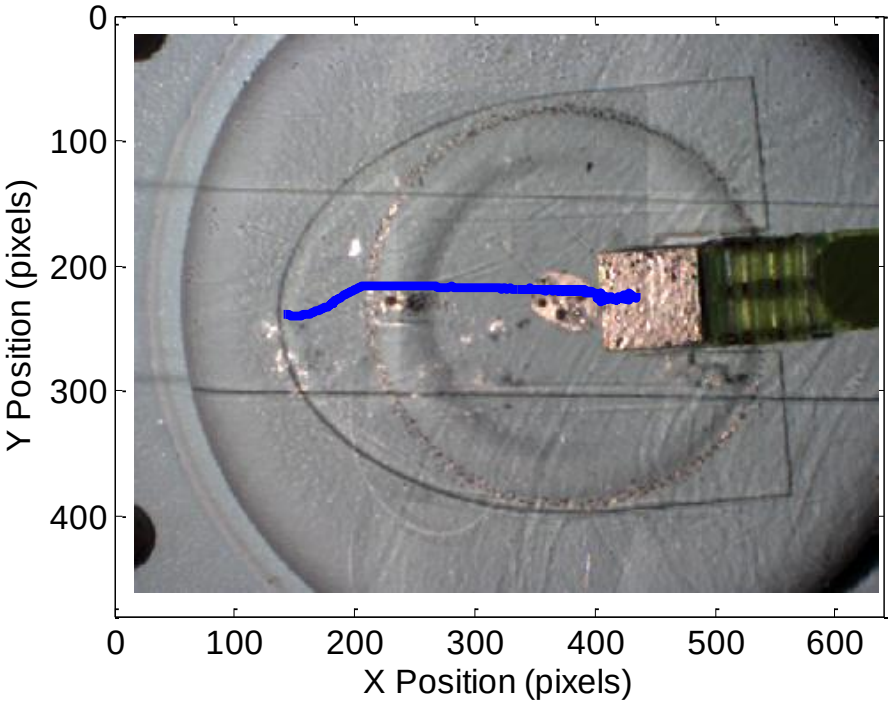

Figure 46: XY position plot of the robot excited at 186 Hz while submerged in the water-glycerine solution with the initial frame of the video underlaid. Note that the robot travels from right-to-left.

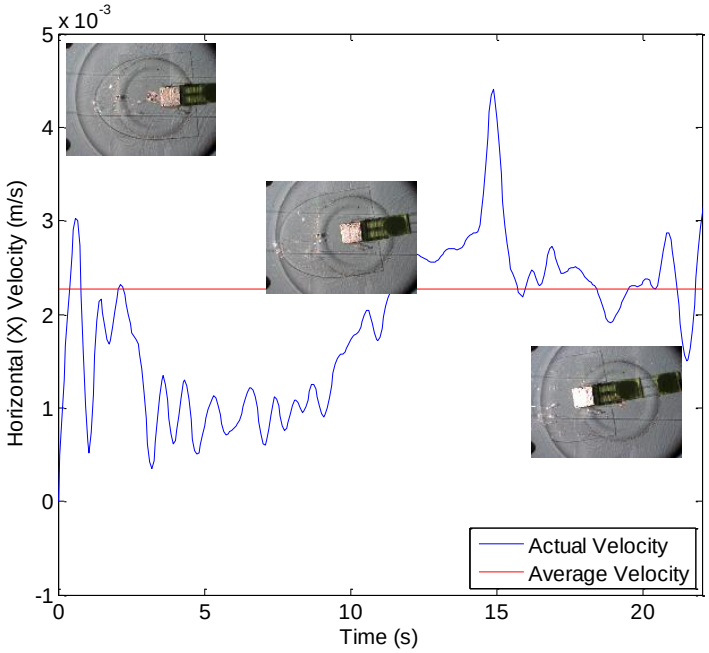

Figure 47: Plot of robot's horizontal velocity vs. time while excited at 186 Hz. Note the actual velocity vs. the average velocity (~2.3 mm/s).

Figure 48 is a plot of the robot's horizontal velocity vs. horizontal position for a portion of time (from ~10s to ~15s). As mentioned above, the robot achieved the best forward progress when the center mass of the robot aligned with the center of the speaker. This is indicated by the horizontal acceleration of the robot, as the velocity increased at a fairly constant rate when passing over the center of the speaker.

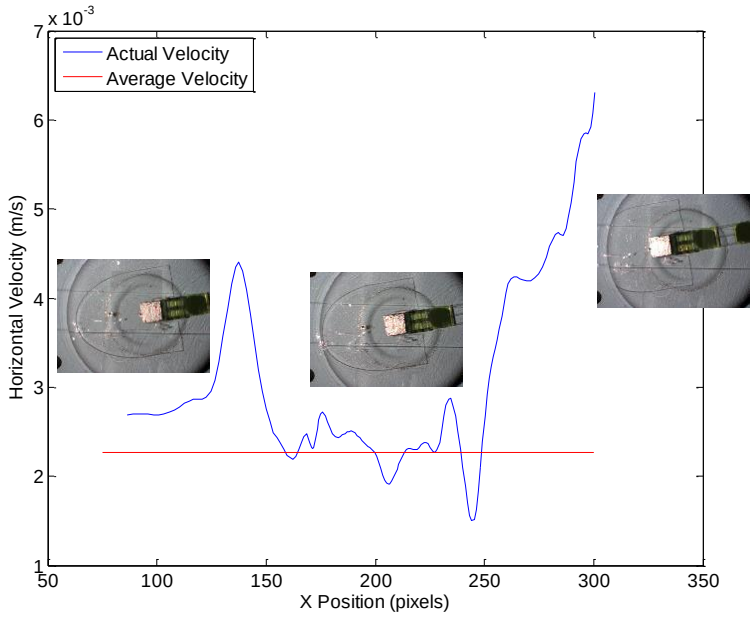

Figure 48: Horizontal velocity vs. position for the robot excited at 186 Hz.

The original robot responded best within the water-glycerine fluid at an input frequency of 186 Hz. At this input, the robot achieved velocities ranging from 1.8 mm/s to 2.3 mm/s depending on the fluid properties. Similar to the behavior exhibited within water, the robot exhibited frequency selectivity as shown in Figure 49. The robot achieved forward propulsion at discrete frequencies, most notably 186 Hz and 130 Hz, which was consistent with the robot's response in water and the COMSOL predictions. Unlike its behavior in water, the robot did not achieve any propulsion at non-resonant frequencies. These successful resonant frequencies were shifted slightly from the predicted values in COMSOL and experimental values in water, but this is to be expected due to the different fluid environment. This result gives further confidence in the idea of achieving a steering mechanism through a pair of alternatively tuned flappers.

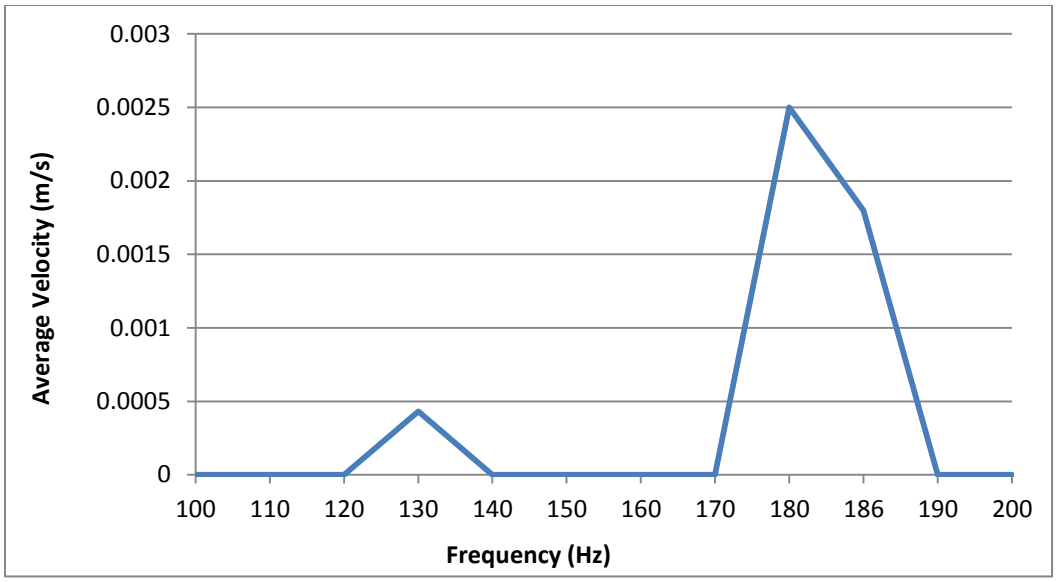

Figure 49: Display of frequency selectivity for robot in water-glycerine solution. Note that the robot responds in a similar manner around its resonant frequencies, but all other frequencies produce no response, unlike water.

A. Small Scale Robot

Further testing involving a scaled down version of the original robot was conducted in order to achieve even lower Reynolds number conditions. The small scale robot, measuring 65 mm x 42 mm x 0.2 mm, was fabricated in the same manner as the original robot and with the same materials. The robot achieved forward propulsion, albeit at a lower velocity (~1.5 mm/s) than the original robot, for a Reynolds number of 4.4. Figure 50 shows the robot's XY position, Figure 51 shows the robot's horizontal velocity vs. time, and Figure 52 shows the robot's horizontal velocity vs. position.

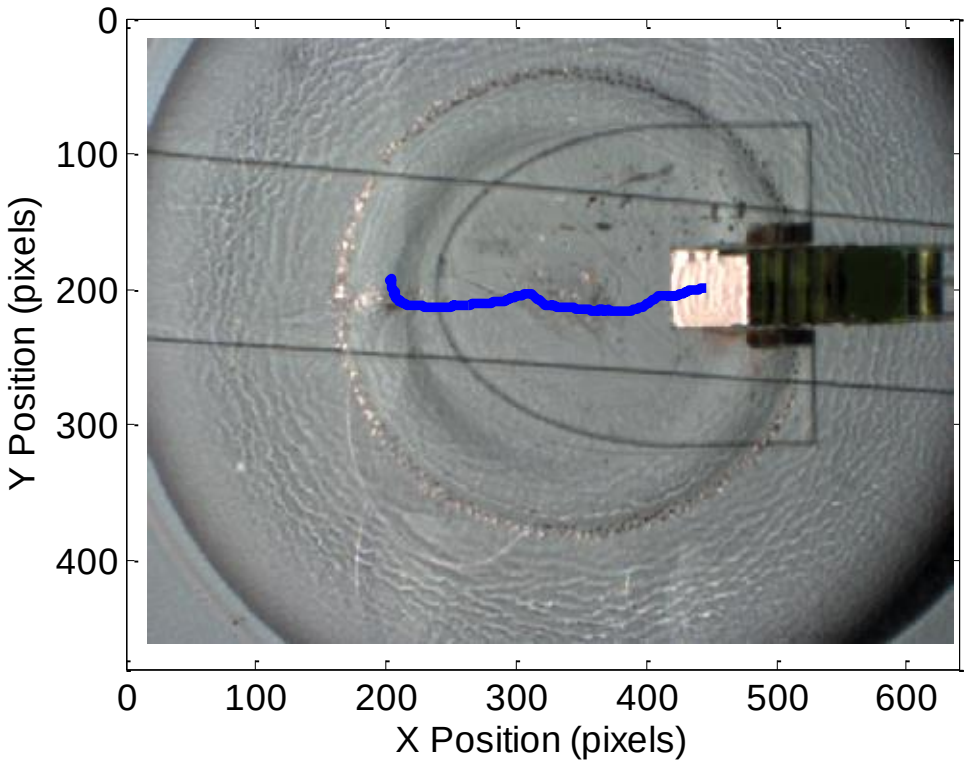

Figure 50: XY Position plot of the small scale robot excited 145 Hz while submerged in the water-glycerine solution. Note that the robot travels from right-to-left.

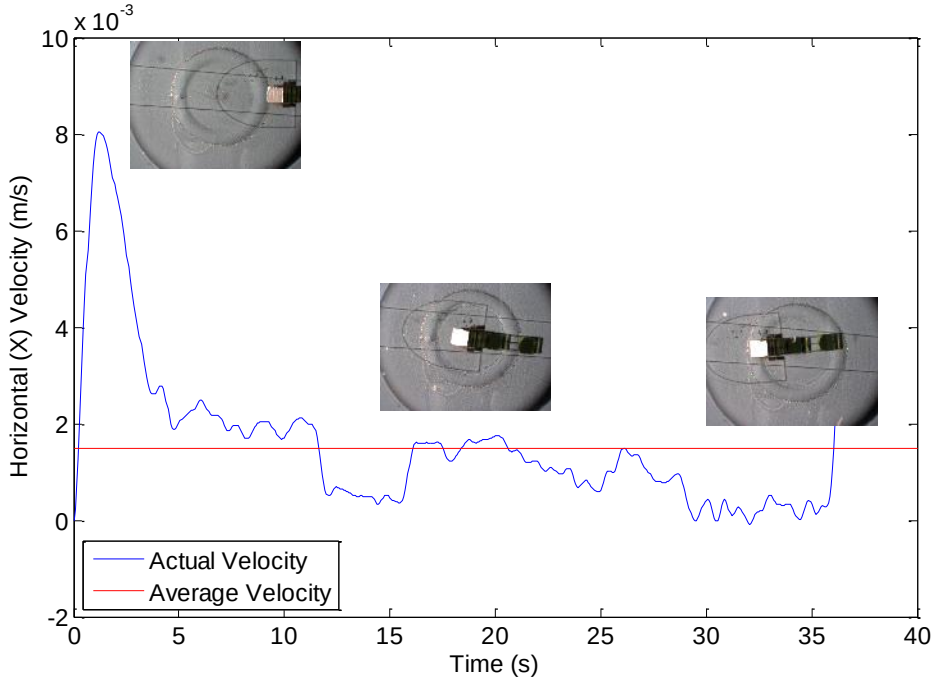

Figure 51: Plot of the small scale robot's horizontal velocity vs. time while excited at 145 Hz. Note the actual velocity vs. the average velocity (~1.5 mm/s).

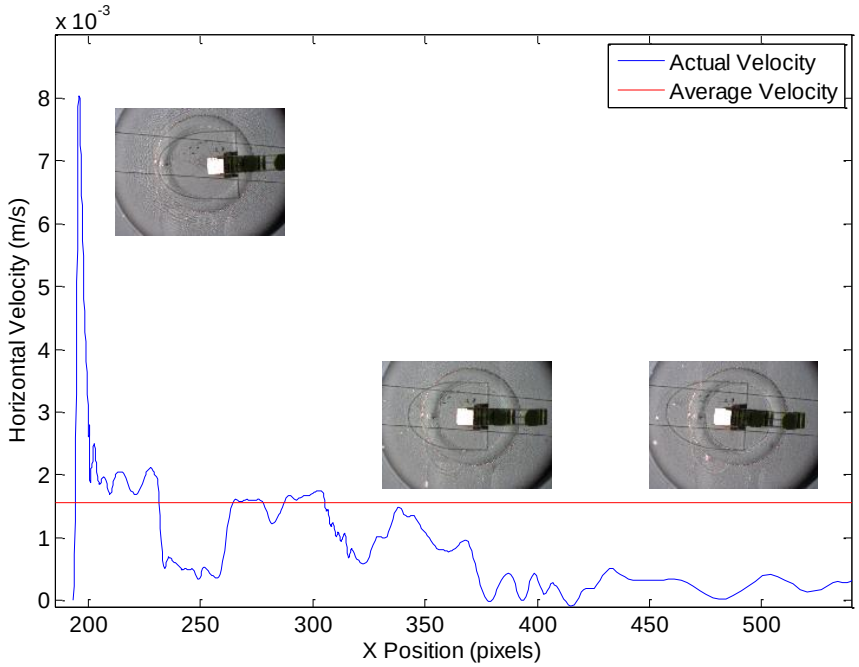

Figure 52: Horizontal velocity vs. position for the small scale robot excited at 145 Hz. Note that the robot does not accelerate over the center of the speaker.

Unlike the original robot, the small scale robot did not accelerate over the center of the speaker in the same manner. While there are several factors that could have contributed to this, one possible explanation is the reduced surface area of the small scale robot. The surface area of the small scale robot was approximately 50% less than the original robot, which could have produced poor coupling between the acoustic field and the robot during its propulsive state.

IX. Contributions

The contributions of the project are as follows:

- Working COMSOL model of flapper
- Validation of COMSOL flapper model with experimental testing
- Flapper capable of non-reciprocal motion
- Working COMSOL model of robot
- Robot capable of propulsion in water
- Robot capable of propulsion at Reynolds numbers as low as 4.4

X. Follow-on Work

The working COMSOL model was useful in terms of designing a structure capable of non-reciprocal motion and getting a rough prediction of its physical behavior. However, a time dependent model within COMSOL would further aid in design and prediction of actual behavior. Being able to determine the robot's predicted behavior in time, as opposed to simply its

eigenmodes, would aid in designing structures that respond in an optimal manner to the interactions between the fluidic environment and acoustic source. Thus, the robot design could be optimized for higher performance, and its behavior could be predicted in various environments with a working time-dependent COMSOL model.

Given the robot's display of frequency selectivity, there is potential to create a steering mechanism using two alternatively tuned flappers. With two flappers that respond to different input frequencies, there would be a different rate of oscillation for each flapper at a given frequency. This difference would necessitate, in a very basic sense, that one side of the robot is propelled forward at a faster rate than the other side, thus turning the robot. In order to create linear motion, there would be a frequency that would allow for the flappers to reach the same rate of oscillation, thus creating solely linear motion. Figure 53 shows a graphical display of this theoretical concept.

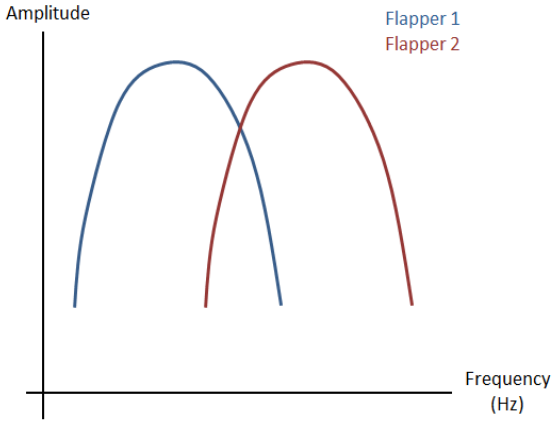

Figure 53: An example of the flapper oscillation amplitude varied over a range of frequencies, for two different flappers. Theoretically, the robot would move forward at the intersection of the two curves, and turn right/left on either side.

Finally, follow-on work pursuing a true microscale robot would bring the project goal to fruition. The time-dependent model would aid in such a task as it could help predict the effects of scaling down the working milliscale robot. Scaling the robot to the microscale would present new challenges in terms of fabrication and testing. More powerful imaging technology would be necessary to track the movement of a microscale object. There is great potential with this project as its success at the milliscale gives confidence to such a concept working at the microscale.

XI. Conclusions

It has been shown that the flapper design implemented in COMSOL is capable of achieving the non-reciprocal mode shapes necessary for propulsion in a low Reynolds number environment. The working COMSOL model provided accurate results in predicting these mode shapes and their frequency location yet will need to be modified in order to create an accurate time-dependent model. This model helped in transitioning from flapper testing to robot design, as it allowed for insight in terms of what structures achieved the best coupling with the acoustic field.

Once a robot design was achieved, the structure was fabricated and tested in water and a more viscous water-glycerine solution to achieve Reynolds numbers as low as 4.4. The robot displayed

frequency selectivity in both environments while achieving forward velocities ranging from 1.5 mm/s to 2.3 mm/s. While the robot's Reynolds number never reached the desired conditions for microscale environment simulations, the robot test results were successful. The robot was tested in a varying fluid regime, with fluid viscosities that increased by two orders of magnitude (10^{-4} Pa·s for water, 10^{-2} Pa·s for the water-glycerine solution) from water's nominal viscosity, while maintaining a forward velocity on the same order of magnitude (mm/s). Ultimately, while further testing will be conducted to confirm the robot's propulsion ability at a true low Reynolds number environment, the current test results indicate that the robot is capable of forward propulsion in increasingly viscous solutions. This, in combination with the follow-on work to leverage a steering mechanism and scaling the robot to the microscale, indicate that this field and project has great potential for development.

XII. References

[1] P. Ball. (2009). *Feynman's Fancy* [online]. Available FTP: http://www.rsc.org/chemistryworld/Issues/2009/January/FeynmansFancy.asp

[2] H. Li *et al*. *Dynamics Modeling and Analysis of a Swimming Microrobot for Controlled Drug Delivery* [online]. Available FTP: http://ieeexplore.ieee.org/stamp/stamp.jsp?tp=&arnumber=4483853

[3] B. Nelson *et al*. *Microrobots for Minimally Invasive Medicine* [online]. Available FTP: http://www.iris.ethz.ch/msrl/publications/files/Nelson_ARBE.pdf

[4] W. Wang *et al*, "Autonomous Motion of Metallic Microrods Propelled by Ultrasound," *ACS Nano*, vol. 6, No. 7, pp. 22-32, 2012

[5] B.J. Nelson *et al*. *How Should Microrobots Swim* [online]. Available FTP: http://www.eng.utah.edu/~jabbott/pmwiki/uploads/Main/Abbott_ISRR07.pdf

[6] A.C.H. Tan and F. S. Hover. *Ultrasonic Thruster* [online]. Available FTP: http://cdn.intechopen.com/pdfs/31683/InTech-Ultrasonic_thruster.pdf

[7] C. Pawashe *et al*. *Modeling and Experimental Characterization of an Untethered Magnetic Micro-robot* [online]. Available FTP: http://ijr.sagepub.com/content/early/2009/07/01/0278364909341413.full.pdf+html

[8] C. Pawasha *et al*. *Multiple Magnetic Microrobot Control Using Electrostatic Anchoring* [online]. Available FTP: http://nanolab.me.cmu.edu/publications/papers/PawasheFloyd-APL09.pdf

[9] Qiu, F., Zhang, L., Tottori, S., Marquardt, K., Krawczyk, K., Franco-Obregón, A., Nelson, B.J., "Bio-inspired microrobots", *Materials Today (Elsevier)*, Vol. 15, p. 463 (2012).

[10] A. Denisov and E. Yeatman. Densive and Yeatman. *Micromechanical Actators Driven By Ultrasonic Power Transfer* [online]. Available FTP: http://ieeexplore.ieee.org/stamp/stamp.jsp?tp=&arnumber=6607214

[11] P. Dariot *et al*. *Microactuators for Microrobots: A Critical Survey* [online]. Available FTP: http://iopscience.iop.org/0960-1317/2/3/005/pdf/0960-1317_2_3_005.pdf

[12] E. M. Purcell, "Life at low Reynolds number," Amer. J. Phys., vol. 45, pp. 3–11, 1976.

[13] B. Nelson, "Microrobots: Liquid," Institute of Robotics and Intelligent Systems, pp. 17-18.

[14] J. H. Mathews. (2003). *Study of Spring-Mass Systems* [online]. Available FTP: http://math.fullerton.edu/mathews/n2003/SpringMassMod.html

[15] P. M. Morse and K. U. Ingard, *Theoretical Acoustics*. Princeton, NJ: Princeton University Press, 1968.

[16] "Modulus of Elasticity." *The Engineering Toolbox*. Internet: http://www.engineeringtoolbox.com/young-modulus-d_417.html, [November 17, 2013].

[17] *Linear Phase, DC Accurate, Tunable 10th Order Low Pass Filter* [online]. Available FTP: http://cds.linear.com/docs/en/datasheet/15697fs.pdf